

Water in Star-forming Regions with the *Herschel* Space Observatory (WISH).

I. Overview of Key Program and First Results

E. F. VAN DISHOECK,^{1,2} L. E. KRISTENSEN,¹ A. O. BENZ,³ E. A. BERGIN,⁴ P. CASELLI,^{5,6} J. CERNICARO,⁷ F. HERPIN,⁸
 M. R. HOGERHEIJDE,¹ D. JOHNSTONE,^{9,10} R. LISEAU,¹¹ B. NISINI,¹² R. SHIPMAN,¹³ M. TAFALLA,¹⁴ F. VAN DER TAK,^{13,15}
 F. WYROWSKI,¹⁶ Y. AIKAWA,¹⁷ R. BACHILLER,¹⁴ A. BAUDRY,⁸ M. BENEDETTINI,¹⁸ P. BJERKELI,¹¹ G. A. BLAKE,¹⁹
 S. BONTEMPS,⁸ J. BRAINE,⁸ C. BRINCH,¹ S. BRUDERER,³ L. CHAVARRÍA,⁸ C. CODELLA,⁶ F. DANIEL,⁷ TH. DE GRAAUW,¹³
 E. DEUL,¹ A. M. DI GIORGIO,¹⁸ C. DOMINIK,^{20,21} S. D. DOTY,²² M. L. DUBERNET,^{23,24} P. ENCRENAZ,²⁵ H. FEUCHTGRUBER,²
 M. FICH,²⁶ W. FRIESWIJK,¹³ A. FUENTE,²⁷ T. GIANNINI,¹² J. R. GOICOECHEA,⁷ F. P. HELMICH,¹³ G. J. HERCZEG,² T. JACQ,⁸
 J. K. JØRGENSEN,²⁸ A. KARSKA,² M. J. KAUFMAN,²⁹ E. KETO,³⁰ B. LARSSON,³¹ B. LEFLOCH,³² D. LIS,³³ M. MARSEILLE,¹³
 C. MCCOEY,^{26,34} G. MELNICK,³⁰ D. NEUFELD,³⁵ M. OLBERG,¹¹ L. PAGANI,²⁵ O. PANIĆ,³⁶ B. PARISE,¹⁶
 J. C. PEARSON,³⁷ R. PLUME,³⁸ C. RISACHER,¹³ D. SALTER,¹ J. SANTIAGO-GARCÍA,³⁹
 P. SARACENO,¹⁸ P. STÄUBER,³ T. A. VAN KEMPEN,¹ R. VISSER,¹ S. VITI,⁴⁰
 M. WALMSLEY,⁶ S. F. WAMPFLER,³ AND U. A. YILDIZ¹

Received 2010 October 18; accepted 2010 December 14; published 2011 February 11

ABSTRACT. Water In Star-forming regions with *Herschel* (WISH) is a key program on the *Herschel Space Observatory* designed to probe the physical and chemical structures of young stellar objects using water and related molecules and to follow the water abundance from collapsing clouds to planet-forming disks. About 80 sources are targeted, covering a wide range of luminosities—from low ($<1 L_{\odot}$) to high ($>10^5 L_{\odot}$)—and a wide range of evolutionary stages—from cold prestellar cores to warm protostellar envelopes and outflows to disks around young stars. Both the HIFI and PACS instruments are used to observe a variety of lines of H_2O , H_2^{18}O and chemically related species at the source position and in small maps around the protostars and selected outflow positions. In addition, high-frequency lines of CO, ^{13}CO , and C^{18}O are obtained with *Herschel* and are complemented by ground-based observations of dust continuum, HDO, CO and its isotopologs, and other molecules to ensure

¹ Leiden Observatory, Leiden University, P.O. Box 9513, 2300 RA Leiden, The Netherlands; ewine@strw.leidenuniv.nl.

² Max-Planck-Institut für Extraterrestrische Physik, Giessenbachstrasse 1, 85748 Garching, Germany.

³ Institute of Astronomy, ETH Zurich, 8093 Zurich, Switzerland.

⁴ Department of Astronomy, University of Michigan, 500 Church Street, Ann Arbor, MI 48109-1042.

⁵ School of Physics and Astronomy, University of Leeds, Leeds LS2 9JT, UK.

⁶ INAF—Osservatorio Astrofisico di Arcetri, Largo E. Fermi 5, 50125 Firenze, Italy.

⁷ Centro de Astrobiología, Departamento de Astrofísica, CSIC-INTA, Carretera de Ajalvir, Km 4, Torrejón de Ardoz. 28850, Madrid, Spain.

⁸ Université de Bordeaux, Laboratoire d’Astrophysique de Bordeaux, France; CNRS/INSU, UMR 5804, Floirac, France.

⁹ National Research Council Canada, Herzberg Institute of Astrophysics, 5071 West Saanich Road, Victoria, BC V9E 2E7, Canada.

¹⁰ Department of Physics and Astronomy, University of Victoria, Victoria, BC V8P 1A1, Canada.

¹¹ Department of Radio and Space Science, Chalmers University of Technology, Onsala Space Observatory, 439 92 Onsala, Sweden.

¹² INAF—Osservatorio Astronomico di Roma, 00040 Monte Porzio catone, Italy.

¹³ SRON Netherlands Institute for Space Research, PO Box 800, 9700 AV, Groningen, The Netherlands.

¹⁴ Observatorio Astronómico Nacional (IGN), Calle Alfonso XII,3. 28014, Madrid, Spain.

¹⁵ Kapteyn Astronomical Institute, University of Groningen, PO Box 800, 9700 AV, Groningen, The Netherlands.

¹⁶ Max-Planck-Institut für Radioastronomie, Auf dem Hügel 69, 53121 Bonn, Germany.

¹⁷ Department of Earth and Planetary Sciences, Kobe University, Nada, Kobe 657-8501, Japan.

¹⁸ INAF—Istituto di Fisica dello Spazio Interplanetario, Area di Ricerca di Tor Vergata, via Fosso del Cavaliere 100, 00133 Roma, Italy.

¹⁹ California Institute of Technology, Division of Geological and Planetary Sciences, MS 150-21, Pasadena, CA 91125, USA.

²⁰ Astronomical Institute Anton Pannekoek, University of Amsterdam, Kruislaan 403, 1098 SJ Amsterdam, The Netherlands.

²¹ Department of Astrophysics/IMAPP, Radboud University Nijmegen, P.O. Box 9010, 6500 GL Nijmegen, The Netherlands.

²² Department of Physics and Astronomy, Denison University, Granville, OH, 43023.

²³ Université Pierre et Marie Curie, LPMMA UMR CNRS 7092, Case 76, 4 place Jussieu, 75252 Paris Cedex 05, France.

²⁴ Observatoire de Paris-Meudon, LUTH UMR CNRS 8102, 5 place Jules Janssen, 92195 Meudon Cedex, France.

²⁵ LERMA and UMR 8112 du CNRS, Observatoire de Paris, 61 Av. de l’Observatoire, 75014 Paris, France.

²⁶ University of Waterloo, Department of Physics and Astronomy, Waterloo, Ontario, Canada.

²⁷ Observatorio Astronómico Nacional, Apartado 112, 28803 Alcalá de Henares, Spain

²⁸ Centre for Star and Planet Formation, Natural History Museum of Denmark, University of Copenhagen, Øster Voldgade 5-7, DK-1350 Copenhagen K, Denmark.

a self-consistent data set for analysis. An overview of the scientific motivation and observational strategy of the program is given, together with the modeling approach and analysis tools that have been developed. Initial science results are presented. These include a lack of water in cold gas at abundances that are lower than most predictions, strong water emission from shocks in protostellar environments, the importance of UV radiation in heating the gas along outflow walls across the full range of luminosities, and surprisingly widespread detection of the chemically related hydrides OH^+ and H_2O^+ in outflows and foreground gas. Quantitative estimates of the energy budget indicate that H_2O is generally not the dominant coolant in the warm dense gas associated with protostars. Very deep limits on the cold gaseous water reservoir in the outer regions of protoplanetary disks are obtained that have profound implications for our understanding of grain growth and mixing in disks.

Online material: color figures

1. INTRODUCTION

As interstellar clouds collapse to form new stars, part of the gas and dust are transported from the infalling envelope to the rotating disk out of which new planetary systems may form (Shu et al. 1987). Water has a pivotal role in these protostellar and protoplanetary environments (see reviews by Cernicharo & Crovisier 2005 and Melnick 2009). As a dominant form of oxygen, the most abundant element in the universe after H and He, it controls the chemistry of many other species, whether in gaseous or solid phase. It is a unique diagnostic of warm gas and energetic processes taking place during star formation. In cold regions, water is primarily in solid form, and its presence as an ice may help the coagulation process that ultimately produces planets. Asteroids and comets containing ice have likely delivered most of the water to our oceans on Earth, where water is directly associated with the emergence of life. Water also contributes to the energy balance as a gas coolant, allowing clouds to collapse up to higher temperatures. The distribution of water vapor and ice during the entire star- and planet-formation processes is therefore a fundamental question relevant to our own origins.

The importance of water as a physical diagnostic stems from the orders-of-magnitude variations in its gas-phase abundance between warm and cold regions (e.g., Cernicharo et al. 1990; van Dishoeck & Helmich 1996; Ceccarelli et al. 1996; Harwit et al. 1998; Ceccarelli et al. 1999; Snell et al. 2000; Nisini et al. 2002; Maret et al. 2002; Boonman et al. 2003; van der Tak et al. 2006). Thus, water acts like a switch that turns on whenever

energy is deposited in molecular clouds and elucidates key episodes in the process of stellar birth; in particular, when the system exchanges matter and energy with its environment. This includes basic stages like gravitational collapse, outflow injection, and stellar heating of disks and envelopes. Its unique ability to act as a natural filter for warm gas and to probe cold gas in absorption make water a highly complementary diagnostic to the commonly used CO molecule.

Studying water is also central to understanding the fundamental processes of freeze-out, grain surface chemistry, and evaporation (e.g., Hollenbach et al. 2009). Water is the dominant ice constituent and can trap various molecules inside its matrix, including complex organic ones (e.g., Gibb et al. 2004b; Boogert et al. 2008). When and where water evaporates back into the gas is therefore relevant for understanding the wealth of organic molecules observed near protostars (see review by Herbst & van Dishoeck 2009). Young stars also emit copious UV radiation and X-rays that affect the physical structure and the chemistry: in particular, that of hydrides like water (Stäuber et al. 2006). Moreover, the level of deuteration of water provides an important record of the temperature history of the cloud and the conditions during grain surface formation, and, in comparison with cometary data, of its evolution from interstellar clouds to solar system objects (e.g., Jacq et al. 1990; Gensheimer et al. 1996; Helmich et al. 1996; Parise et al. 2003).

Finally, water plays an active role in the energy balance of dense gas (e.g., Goldsmith & Langer 1978; Neufeld & Kaufman 1993; Doty & Neufeld 1997). Because water has a large dipole

²⁹ Department of Physics and Astronomy, San Jose State University, One Washington Square, San Jose, CA 95192.

³⁰ Harvard-Smithsonian Center for Astrophysics, 60 Garden Street, MS 42, Cambridge, MA 02138.

³¹ Department of Astronomy, Stockholm University, AlbaNova, 106 91 Stockholm, Sweden.

³² Laboratoire d'Astrophysique de Grenoble, CNRS/Université Joseph Fourier (UMR5571) BP 53, F-38041 Grenoble Cedex 9, France.

³³ California Institute of Technology, Cahill Center for Astronomy and Astrophysics, MS 301-17, Pasadena, CA 91125.

³⁴ University of Western Ontario, Department of Physics & Astronomy, London, Ontario, Canada N6A 3K7.

³⁵ Department of Physics and Astronomy, Johns Hopkins University, 3400 North Charles Street, Baltimore, MD 21218.

³⁶ European Southern Observatory, Karl-Schwarzschild-Str. 2, 85748 Garching, Germany.

³⁷ Jet Propulsion Laboratory, California Institute of Technology, Pasadena, CA 91109.

³⁸ Department of Physics and Astronomy, University of Calgary, Calgary, T2N 1N4, AB, Canada.

³⁹ Instituto de RadioAstronomía Milimétrica, Avenida Divina Pastora, 7, Núcleo Central E 18012 Granada, Spain.

⁴⁰ Department of Physics and Astronomy, University College London, Gower Street, London WC1E6BT, UK.

moment, its emission lines can be efficient coolants of the gas, contributing significantly over the range of physical conditions that are appropriate in star-forming regions. The large dipole moment can also lead to heating through absorption of infrared radiation, followed by collisional deexcitation (Ceccarelli et al. 1996). It is therefore important to study the gaseous water emission and absorption and to compare its cooling or heating efficiency quantitatively with that of other species.

Interstellar water was detected more than 40 years ago through its 22 GHz maser emission toward Orion (Cheung et al. 1969). While this line remains a useful beacon of star-formation activity, its special excitation and line-formation conditions limit its usefulness as a quantitative physical and chemical tool. Because observations of thermally excited water lines from Earth are limited, most information on water has come from satellites. The *Submillimeter Wave Astronomy Satellite* (SWAS; Melnick et al. 2000) and the Odin satellite (e.g., Hjalmarson et al. 2003; Bjerkeli et al. 2009) observed only the 557 GHz ground-state line of ortho- H_2O at spatial resolutions of $\sim 3.3' \times 4.5'$ and $126''$, respectively. The 557 GHz line was detected in just the brightest objects by these missions, and other lines of water (including those of para- H_2O) and related species could not be observed. The short-wavelength spectrometer (SWS) and long-wavelength spectrometer (LWS) on the *Infrared Space Observatory* (ISO) covered a large number of pure rotational and vibrational-rotational lines, providing important insight into the water excitation and distribution, but with limited spectral and spatial resolution and mapping capabilities (see the review by van Dishoeck 2004). The *Spitzer Space Telescope* has detected highly excited pure rotational H_2O lines at mid-infrared wavelengths from shocks (Melnick et al. 2008; Watson et al. 2007) and from the inner few AU regions of protoplanetary disks (Salyk et al. 2008; Carr & Najita 2008; Pontoppidan et al. 2010). Even higher-lying vibrational-rotational H_2O lines have been observed at near-infrared wavelengths from the ground (Salyk et al. 2008). However, these data do not provide any information on the cooler water reservoir where the bulk of the disk mass is located.

The 3.5 m *Herschel Space Observatory* with its suite of instruments (Pilbratt et al. 2010)⁴¹ is particularly well suited to address the distribution of cold and warm water in star- and planet-forming regions, building on the pioneering results from previous missions. Its wavelength coverage of 55–671 μm (0.45–5.4 THz; 15–180 cm^{-1})⁴² includes both low- and high-excitation lines of water, enabling a detailed analysis of its excitation and abundance structure (Fig. 1). Compared

with the ISO-LWS beam ($\sim 80''$), *Herschel* has a gain of a factor of ~ 8 in spatial resolution at similar wavelengths and up to 10^4 in spectral resolution. Compared with observatories with high spectral resolution heterodyne instruments, its diffraction-limited beam of $37''$ at 557 GHz is a factor of 3–5 smaller than that of SWAS or Odin, with a gain of >10 in sensitivity because of the bigger dish and improved detector technology. The Heterodyne Instrument for the Far-Infrared (HIFI; de Graauw et al. 2010) has spectral resolving powers $R = \lambda/\Delta\lambda > 10^7$ up to 1900 GHz, allowing the kinematics of the water lines to be studied. The Photoconducting Array Camera and Spectrometer (PACS; Poglitsch et al. 2010) 5×5 pixel array provides instantaneous spectral mapping capabilities at $R = 1500\text{--}4000$ of important (backbone) water lines in the 55–200 μm range. These enormous advances in sensitivity, spatial and spectral resolution, and wavelength coverage provide a unique opportunity to observe both cold and hot water in space, with no other space mission with similar capabilities being planned.

The goal of the Water In Star-forming regions with *Herschel* (WISH) key program (KP) is to use gas-phase water as a physical and chemical diagnostic and follow its abundance throughout the different phases of star and planet formation. A comprehensive set of water observations is carried out with HIFI and PACS toward a large sample of young stellar objects (YSOs), covering a wide range of masses and luminosities—from the lowest to the highest mass protostars—and a large range of evolutionary stages—from the first stages represented by the prestellar cores to the late stages represented by the pre-main-sequence stars surrounded only by disks. Lines of H_2O , H_2^{18}O , and H_2^{17}O and the chemically related species O, OH, and H_3O^+ are targeted.⁴³ In addition, a number of hydrides that are diagnostic of the presence of X-rays and UV radiation are observed. Selected high-frequency lines of CO, ^{13}CO , and C^{18}O , as well as dust continuum maps, are obtained to constrain the physical structure of the sources, independently of the chemical effects. Together with the atomic O and C^+ lines, these data also constrain the contributions from the major coolants. The *Herschel* data are complemented by ground-based maps of longer-wavelength continuum emission and lines of HDO, CO, C, and other molecules to ensure a self-consistent data set for analysis. In terms of water, the WISH program is complementary to the Chemical Survey of Star-forming Regions (CHESS; Ceccarelli et al. 2010) and *Herschel* Observations of Extraordinary Sources (HEXOS; Bergin et al. 2010b) HIFI KPs that survey the entire spectral range (including many lines of water), but only for a limited number of sources and with smaller on-source integration times per frequency setting. The Dust, Ice, and Gas in Time (DIGIT; PI N.J. Evans) and *Herschel* Orion Protostar Survey (HOPS; PI T. Megeath) KPs complement

⁴¹ *Herschel* is an ESA space observatory with science instruments provided by European-led Principal Investigator consortia and with important participation from NASA.

⁴² This article follows the common usage of giving frequencies in gigahertz for lines observed with HIFI and giving wavelengths in microns for lines observed with PACS.

⁴³ Both H_2O and water are used to denote the main H_2^{16}O isotopolog throughout this article.

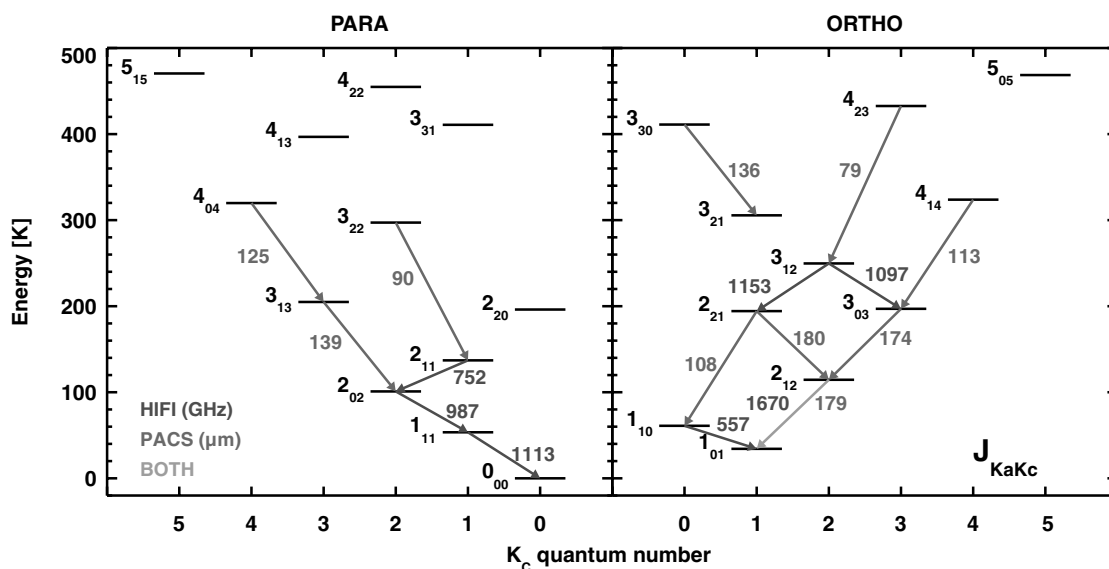


FIG. 1.—Energy levels of ortho- and para- H_2O , with HIFI transitions (in gigahertz) and PACS transitions (in microns) observed in WISH indicated. See the electronic edition of the *PASP* for a color version of this figure.

WISH by carrying out full PACS spectral scans for a larger sample of low-mass embedded YSOs (e.g., van Kempen et al. 2010a). The Probing Interstellar Molecules with Absorption Line Studies (PRISMAS) KP targets the water chemistry in the diffuse interstellar gas (Gerin et al. 2010), whereas Water and Related Chemistry in the Solar System (also known as Herschel Solar System Observations [HssO]) observes water in planets and comets (Hartogh et al. 2010). Together, these *Herschel* data on water and related hydride lines will provide a legacy for decades to come.

In the following sections, background information on the water chemistry and excitation relevant for interpreting the data is provided (§ 2). The observational details and organization of the WISH program are subsequently described in § 3, with the specific goals and first results of the various subprograms presented in § 4. A discussion of the results across the various evolutionary stages and luminosities is contained in § 5, together with implications for the water chemistry, with conclusions in § 6. Detailed information can be found at the WISH KP World Wide Web site.⁴⁴ This Web site includes links to model results, modeling tools, complementary data, and outreach material. These data and analysis tools will be useful not only for *Herschel* but also for planning observations with the Atacama Large Millimeter/submillimeter Array (ALMA) and future far-infrared missions.

2. H_2O CHEMISTRY AND EXCITATION

Star formation takes place in cold dense cores with temperatures around 10 K and H_2 densities of at least 10^4 cm^{-3} . Once collapse starts and a protostellar object has formed, its central luminosity heats the surrounding envelope to temperatures well above 100 K. Moreover, bipolar jets and winds interact with the envelope and cloud, creating shocks in which the temperature is raised to several thousand degrees Kelvin. Cloud core rotation leads to a circumstellar disk around the young star, with densities in the midplane of $>10^{10} \text{ cm}^{-3}$. With time, the envelope is dispersed by the action of the outflow, leaving the pre-main-sequence star with a disk only. Once accretion onto the disk stops and the disk becomes less turbulent, the $\sim 0.1 \mu\text{m}$ grains from the collapsing cloud coagulate to larger particles and settle to the midplane, eventually leading to planetesimals and (proto) planets. Thus, star-forming regions contain gas with a large range of temperatures and densities, from 10 to 2000 K and 10^4 to $>10^{10} \text{ cm}^{-3}$, and with gas/dust ratios that may vary from the canonical value of 100 to much larger or smaller values. The water chemistry responds to these different conditions.

2.1. Chemistry

Figure 2 contains an overview of the physical structure of a typical protostellar envelope, with the main chemical regimes indicated. In standard gas-phase chemistry, H_2O forms through ion-molecule reactions starting with $\text{O} + \text{H}_3^+$ and $\text{O}^+ + \text{H}_2$, both leading to OH^+ (e.g., Herbst & Klemperer 1973; Dalgarno & Black 1976) (see Fig. 3). A series of rapid hydrogen abstraction reactions with H_2 leads to H_3O^+ , which can dissociatively

⁴⁴ See <http://www.strw.leidenuniv.nl/WISH/>.

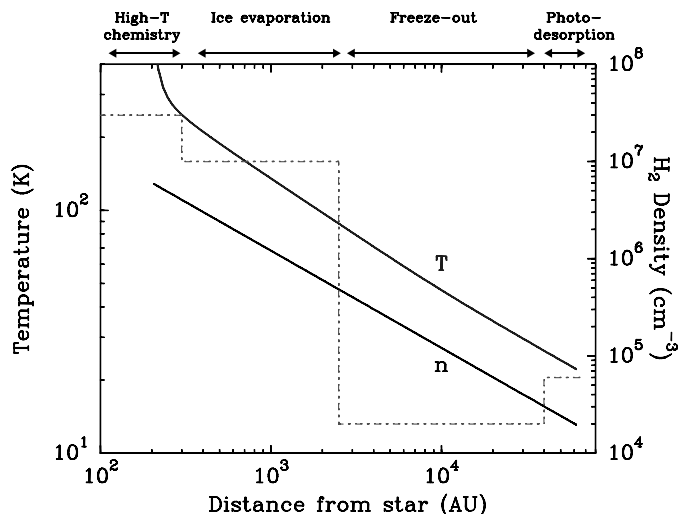


FIG. 2.—Temperature and density structure of a high-mass protostellar envelope. For illustrative purposes, a typical abundance profile is included (dash-dotted line) on an arbitrary scale, with the relevant chemical processes in each regime indicated at the top of the figure. The figure is based on the model of AFGL 2591 ($L = 6 \times 10^4 L_{\odot}$) presented by van der Tak et al. (1999). For distances of ~ 1 kpc, the typical *Herschel* beam of $20''$ corresponds to 20,000 AU; i.e., it encompasses the entire envelope. For low-mass protostars, the ice evaporation zone moves inward to radii typically less than 100 AU. See the electronic edition of the *PASP* for a color version of this figure.

recombine to form H_2O and OH with branching ratios of $\sim 33\%$ and 66% , respectively (Vejby-Christensen et al. 1997). H_2O is destroyed by ultraviolet photons and by reactions with C^+ , H_3^+ , and other ions such as HCO^+ . All key reactions in this network have been measured or calculated at low temperatures (e.g., Klippenstein et al. 2010). The steady-state H_2O abundance resulting from pure gas-phase chemistry is typically a few times 10^{-7} with respect to H_2 at low T and scales with the cosmic-ray ionization rate ζ (e.g., Woodall et al. 2007).

In the last decades, this traditional view of the oxygen chemistry has been radically changed, triggered by the very low abundances of O_2 in cold clouds found by *SWAS* (e.g., Bergin et al. 2000). It is now realized that in cold and dense regions, H_2O is formed much more efficiently on the grains through a series of reactions involving O and H accreted from the gas, as predicted more than 50 years ago by van de Hulst and quantified by Tielens & Hagen (1982). Surface science laboratory experiments are only now starting to test these reactions experimentally (Ioppolo et al. 2008, 2010; Miyauchi et al. 2008; Dulieu et al. 2010; Romanzin et al. 2010). While the details are not yet fully understood (e.g., Cuppen et al. 2010), there is ample observational evidence from $3 \mu\text{m}$ absorption spectroscopy of the solid H_2O band toward YSOs that the H_2O ice abundances can be as high as $\sim 10^{-4}$, much higher than results from freeze-out of gas-phase H_2O (e.g., Whittet et al. 1988; Pontoppidan et al. 2004).

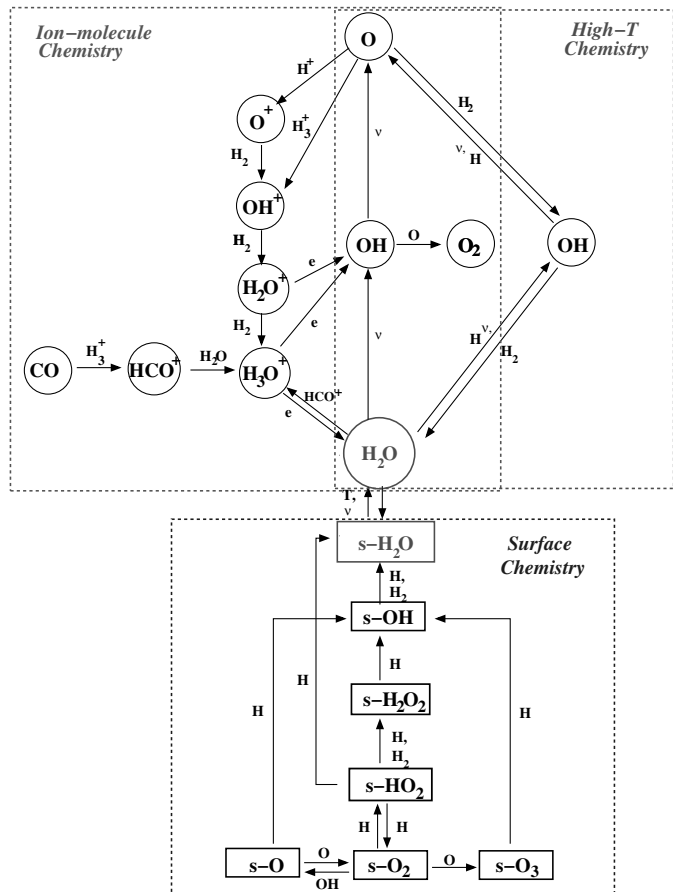


FIG. 3.—Summary of the main gas-phase and solid-state chemical reactions leading to the formation and destruction of H_2O . Three different chemical regimes can be distinguished: (1) ion-molecule chemistry, which dominates gas-phase chemistry at low T ; (2) high-temperature neutral-neutral chemistry; and (3) solid-state chemistry. The latter chemical scheme is based on the latest laboratory data by Ioppolo et al. (2010); $s\text{-}X$ denotes species X on the ice surfaces. See the electronic edition of the *PASP* for a color version of this figure.

Water ice formation starts at a threshold extinction of $A_V \approx 5$ mag: i.e., well before the cloud collapses (Whittet 2003). A small fraction of the H_2O ice formed by surface reactions can be desorbed back into the gas phase by a variety of nonthermal processes, including cosmic-ray-induced desorption and photodesorption (see the recent overview by Hollenbach et al. 2009). The efficiency of the latter process has been quantified by laboratory experiments to be $\sim 10^{-3}$ per incident UV photon (Westley et al. 1995; Öberg et al. 2009).

Near protostars, the grain temperature rises above ~ 100 K and all the H_2O ice thermally desorbs on very short timescales (Fraser et al. 2001), leading to initial gas-phase abundances of H_2O as high as the original ice abundances of $\sim 10^{-4}$. Other molecules trapped in the water ice matrix evaporate at the same time in these so-called hot-core or hot-corino (in the case of low-mass YSOs) regions. Thus, constraining the H_2O evaporation

zone is also critical for the interpretation of complex organic molecules in hot cores.

At even higher temperatures, above 230 K, the gas-phase reaction $\text{O} + \text{H}_2 \rightarrow \text{OH} + \text{H}$, which is endoergic by ~ 2000 K, becomes significant (Elitzur & Watson 1978; Charnley 1997). OH subsequently reacts with H_2 to form H_2O , a reaction that is exothermic but has an energy barrier of ~ 2100 K (Atkinson et al. 2004). This route drives all the available gas-phase oxygen into H_2O , leading to an abundance of $\sim 3 \times 10^{-4}$ at high temperatures, unless the H/H_2 ratio in the gas is so high that the back-reactions become important. Such hot gas can be found in the hot cores close to the protostars themselves and in the more extended shocked gas associated with the outflows. Given the range of temperatures and densities in protostellar (Fig. 2) and protoplanetary environments, all of the preceding chemical processes likely play a role, and the *Herschel* data are needed to determine their relative importance.

H_2O has a unique deuteration pattern compared with other molecules. If grain surface formation dominates, water is deuterated in the ice at a level that may be orders of magnitude lower than that of other species that participate more actively in the dense cold gas chemistry (Roberts et al. 2003). Indeed, the deuteration fraction observed in high-mass hot cores is typically $\text{HDO}/\text{H}_2\text{O} < 10^{-3}$ (e.g., Gensheimer et al. 1996; Helmich et al. 1996), although higher values around 10^{-2} have recently been found for Orion (Persson et al. 2007, Bergin et al. 2010a) and for a low-mass hot core (Parise et al. 2005b). All of these values are still much lower than, for example, DCN/HCN , $\text{HDCO}/\text{H}_2\text{CO}$ (e.g., Loinard et al. 2001), or $\text{CH}_2\text{DOH}/\text{CH}_3\text{OH}$ (Parise et al. 2004). In the solid phase, the $\text{HDO}/\text{H}_2\text{O}$ upper limits are less than 2×10^{-3} (Dartois et al. 2003; Parise et al. 2003). An important question is how similar the protostellar $\text{HDO}/\text{H}_2\text{O}$ ratios are to those observed in comets and in water in our oceans on Earth (about 2×10^{-4}), since this has major implications for the delivery mechanisms of water to our planet (Bockelée-Morvan et al. 1998; Raymond et al. 2004). No specific HDO lines are targeted with *Herschel* within the WISH program, since several HDO lines can be observed from the ground (Parise et al. 2005a). HIFI will provide the necessary data on H_2O itself for comparison with those HDO data.

2.2. Excitation

H_2O is an asymmetric rotor with a highly irregular set of energy levels characterized by quantum numbers $J_{K_A K_C}$. Because of the nuclear spin statistics of the two hydrogen atoms, the H_2O energy levels are grouped into ortho ($K_A + K_C = \text{odd}$) and para ($K_A + K_C = \text{even}$) ladders across which no transitions can occur except through chemical reactions that exchange a H nucleus (Fig. 1). The H_2O energy levels within each ladder are populated by a combination of collisional and radiative processes. The most important collision partners are ortho- and para- H_2 , with electrons and H only significant in specific regions and He contributing at a low level. Accurate

collisional rate coefficients are thus crucial to interpret the *Herschel* data. The bulk of these rates are obtained from theoretical quantum chemistry calculations that involve two steps. First, a multidimensional potential energy surface involving the colliders is computed. Second, the dynamics on this surface are investigated with molecular scattering calculations at a range of collision energies. Early studies used simplifications such as replacing H_2 with He (Green et al. 1993), including only a limited number of degrees of freedom of the colliding system, or using approximations in the scattering calculations (Phillips et al. 1996). Recent calculations consider a 5D potential surface and compute collisions with both para- H_2 and ortho- H_2 separately up to high temperatures with the close coupling method (Dubernet et al. 2009; Daniel et al. 2010). This 5D potential is based on the full 9D potential surface computed by Valiron et al. (2008). The cross sections for collisions of H_2O with *o*- H_2 are found to be significantly larger than those with *p*- H_2 for low J , so that explicit treatment of the *o/p* H_2 ratio is important.

Direct comparison of absolute values of theoretical state-to-state cross sections with experimental data is not possible, but the accuracy of the 9D potential surface has been confirmed implicitly through comparison with other data sets, including differential scattering experiments of H_2O with H_2 (Yang et al. 2010). An indication of the accuracy of the calculations can also be obtained from recent pressure-broadening experiments (Dick et al. 2010). The high-temperature (> 80 K) data agree with theory within 30% or better, but the low-temperature experimental rate coefficients are an order of magnitude smaller. This discrepancy has recently been understood by realizing that the classical impact approximation used in the analysis of the pressure-broadening data does not hold at very low temperatures (Wiesenfeld & Faure 2010). The computed rate coefficients at low T by Dubernet et al. (2006) should therefore be valid.

Because of the large rotation constants of water, the energy spacing between the lower levels is much larger than that of a heavy molecule like CO. Thus, the water transitions couple much more efficiently with far-infrared radiation from warm dust, which can pump higher energy levels (e.g., Takahashi et al. 1983). This far-infrared continuum also plays a role in the line formation (e.g., whether the line occurs in absorption or emission) and thus provides constraints on source geometry. Moreover, the continuum can become optically thick at the highest frequencies, providing an effective screen for looking to different depths in the YSO environment (Poelman & van der Tak 2007; van Kempen et al. 2008).

The high transition frequencies combined with the large dipole moment of H_2O (1.85 D) also lead to high line opacities. For example, for the *o*- H_2O 557 GHz ground-state transition, the line-center optical depth is $\tau_0 = 2.0 \times 10^{-13} N_\ell(o\text{-H}_2\text{O})\Delta V$, where N_ℓ is the column density in the lower level in cm^{-2} , which, to first approximation, is equal to the total *o*- H_2O column density, and ΔV is the FWHM of the line in km s^{-1} (Plume et al. 2004). Thus, even for H_2O abundances

as low as 10^{-9} in typical clouds with $N(\text{H}_2) \geq 10^{22} \text{ cm}^{-2}$, the water lines are optically thick at line center.

Because of the high optical depths, it is difficult to extract reliable water abundances from lines of the main isotopolog. However, because the excitation is subthermal (critical densities are typically $10^8\text{--}10^9 \text{ cm}^{-3}$), every photon that is created will scatter and eventually escape the cloud. In this so-called effectively thin limit, the water column density scales linearly with integrated intensity of a ground-state transition and is inversely proportional to density and the value of the collisional rate coefficient (Snell et al. 2000; Schulz et al. 1991).

Many of the H_2O transitions exhibit population inversion, either very weakly or more strongly, such as the famous $6_{16} - 5_{23}$ maser at 22 GHz that is widely observed in star-forming regions (e.g., Szymczak et al. 2005). Thus, the H_2O molecule forms a formidable challenge for radiative transfer codes, and the HIFI and PACS spectra provide a unique reference data set of thermal lines against which to test the basic assumptions in the maser models.

2.3. Modeling Tools

The WISH team has developed a variety of tools important for the *Herschel* data analysis, several of which are publicly available to the community. This includes a molecular line database LAMDA⁴⁵ for excitation calculations of H_2O , OH, CO, and other molecules using various sets of collisional rate coefficients discussed previously (Schöier et al. 2005). Simple 1D escape probability non-LTE radiative transfer programs such as RADEX can be run either online or downloaded to run at the researcher's own institute (van der Tak et al. 2007). This and the more sophisticated Monte Carlo 1D radiative transfer code RATRAN are publicly available,⁴⁶ and RADEX is also included in the CASSIS set of analysis programs.⁴⁷ The RATRAN code has been extensively tested in a code comparison campaign (van Zadelhoff et al. 2002). Another 1D non-LTE code used by the WISH team is MOLLIE (Keto et al. 2004). A 2D version of RATRAN and a new flexible 3D line radiative transfer code called LIME are available on a collaborative basis (Hogerheijde & van der Tak 2000; Brinch & Hogerheijde 2010). A 2D escape probability code has been written by Poelman & Spaans (2005), and a fast 3D code using a local source approximation has been developed by Bruderer et al. (2010a).

Recognizing the importance and complexity of the radiative transfer problem for H_2O , the HIFI consortium organized a benchmark workshop dedicated to an accurate comparison of radiative transfer codes in 2004. The model tests and results are available on a Web page⁴⁸ so that future researchers can test

new codes. The reliability of existing codes has significantly improved from these efforts.

Predictions of water emission lines have been made for grids of 1D spherically symmetric envelope models over a large range of luminosities, envelope masses, and other YSO parameters, for a range of H_2O abundances (e.g., Poelman & van der Tak 2007; van Kempen et al. 2008). Many of the line profiles show deep absorptions and hornlike shapes, due to the high line-center optical depths discussed previously, with emission only escaping in the line wings.

Chemical models of envelopes and hot cores have been developed for low- and high-mass sources (e.g., Doty et al. 2002, 2004; Viti et al. 2001). In these models, the physical conditions are kept static with time. Models in which the physical structure of the source changes with time as the cloud collapses and the luminosity evolves have been made by Ceccarelli et al. (1996), Viti & Williams (1999), Rodgers & Charnley (2003), Lee et al. (2004), Doty et al. (2006), and Aikawa et al. (2008) in 1D and by Visser et al. (2009) in 2D. Grids of 1D *C*-type shock models by Kaufman & Neufeld (1996) and bow-shock models by Gustafsson et al. (2010) are also available. The effects of high-energy irradiation have been studied in spherical symmetry in a series of articles (Stäuber et al. 2004, 2005, 2006) and have been extended to multidimensional geometries (Bruderer et al. 2009b, 2009a, 2010a).

2.4. Modeling Approach

Spherically symmetric models of protostellar envelopes such as illustrated in Figure 2 are constructed for all sources in the WISH sample by assuming a power-law density profile and calculating the dust temperature with radius using a continuum radiative transfer code such as DUSTY (Ivezić & Elitzur 1997) or RADMC (Dullemond & Dominik 2004), taking the central luminosity as input. The power-law exponent, spatial extent, and envelope dust mass are determined from χ^2 minimization to the far-infrared spectral energy distribution and submillimeter continuum maps (see procedure by Jørgensen et al. 2002). The gas temperature is taken to be equal to the dust temperature, which is a good approximation at these high densities where gas-dust coupling is significant (Doty & Neufeld 1997), and the gas mass density is obtained through multiplication of the dust density by a factor of 100. These models are termed passively heated envelope models, to distinguish them from active shock and UV photon heating mechanisms.

At typical distances of star-forming regions, the warm and cold regions—and thus the H_2O chemistry zones—will be largely spatially unresolved in the *Herschel* beams. However, the abundance variations (where is the water spatially along the line of sight?) can be reconstructed through multiline, single-position observations coupled with physical models of the sources and radiative transfer analyses. This backward-modeling technique for retrieval of the abundance profiles in protostellar envelopes has been demonstrated for ground-based data on a variety of molecules

⁴⁵ See <http://www.strw.leidenuniv.nl/~moldata>.

⁴⁶ See <http://www.sron.rug.nl/~vdtak/ratran/frames.html>.

⁴⁷ http://www.cesr.fr/~walters/web_cassis/.

⁴⁸ See <http://www.sron.rug.nl/~vdtak/H2O>.

such as CO (Jørgensen et al. 2002), CH₃OH (e.g., van der Tak et al. 2000a; Maret et al. 2005; Kristensen et al. 2010a), and H₂CO (e.g., van Dishoeck et al. 1995; Ceccarelli et al. 2000b; Schöier et al. 2002; Maret et al. 2005; Jørgensen et al. 2005b) and confirmed by interferometer data (Jørgensen 2004; Schöier et al. 2004). Asymmetric rotors like H₂O with many lines from different energies close in frequency are particularly well suited for such analyses.

Given a temperature and density structure, the molecular excitation and radiative transfer in the line are computed at each position in the envelope. The resulting sky brightness distribution is convolved with the beam profile. A trial abundance of water is chosen (see the example in Fig. 2) and is adjusted until the best agreement with observational data is reached. The velocity structure is represented either by a turbulent broadening width that is constant with position or by some function: for example, an infall velocity profile.

The alternative forward-modeling approach starts from a full physicochemical model and computes the water emission at different times in the evolution for comparison with observations (see Fig. 1 of Doty et al. 2004 for a flowchart of both procedures). In this case, one obtains best-fit model parameters such as the timescale since evaporation (often labeled as the “age” of the source) or the cosmic-ray ionization rate (e.g., Doty et al. 2006).

The spherically symmetric models are an important first step, but initial *Herschel* results show that they are generally not sufficient to interpret the data. Other components such as shocks or UV-heated cavity walls need to be added in a 2D geometry (van Kempen et al. 2010b; Visser et al. 2011, in preparation).

3. OBSERVATIONS

3.1. Source and Line Selection

The WISH program contains about 80 sources covering a range of luminosities and evolutionary stages and uses about 425 hr of *Herschel* time. The sources are summarized in Table 1, where they are subdivided into a set of subprograms. Multiline pointed observations at the source position are performed using the HIFI and PACS instruments. In addition, small maps over a few-arcminute region are made for selected sources using either the on-the-fly (HIFI) or raster mapping (PACS) strategies. The number of sources per (sub)category ranges from two for the cold line-poor sources to more than 10 for warm line-rich objects—large enough to allow individual source peculiarities to be distinguished from general trends. These deep integrations and thorough coverage of the various types of H₂O lines will set the stage to design future *Herschel* programs of larger, more statistically significant samples using fewer lines. Specific source selection for each subprogram is discussed in § 4. More than 90% of our sources are visible with ALMA ($\delta < 40^\circ$).

The selection of H₂O lines observed with HIFI and PACS is summarized in Figure 1 and Table 2 and is based on information

from existing *ISO*-LWS, *SWAS*, and *Odin* data and on extensive modeling performed for shocks (e.g., Neufeld & Dalgarno 1989; Kaufman & Neufeld 1996; Giannini et al. 2006), low-mass (Ceccarelli et al. 2000a; van Kempen et al. 2008) and high-mass YSO envelopes (Doty & Neufeld 1997; Walmsley & van der Tak 2005; Poelman & van der Tak 2007). Three sets of lines can be distinguished. The ground-state *o*- and *p*-H₂O lines at 557 and 1113 GHz are the prime diagnostics of the cold gas. These and other lines connected with ground-state levels (e.g., $2_{12} - 1_{01}$ at 1670 GHz) usually show strong self-absorption or they can even be purely in absorption against the strong continuum provided by the source itself. The second group are “medium-*J*” lines originating from levels around 100–250 K above ground, which probe the warm gas (e.g., $2_{02} - 1_{11}$ at 988 GHz and $3_{12} - 3_{03}$ at 1097 GHz). The third group are the highly excited lines originating from levels >300 K, which are only populated in strong shocks (e.g., higher-lying backbone lines) or which are anomalously excited by collisional or infrared pumping, leading to maser emission. Because of high optical depths, optically thin isotopic lines are crucial for the interpretation so that deep integrations on a number of H₂¹⁸O and H₂¹⁷O lines are included in the program.

For all deeply embedded YSOs, a common strategy is adopted by observing the ground-state *o*-H₂O $1_{10} - 1_{01}$ 557 GHz and *p*-H₂O $1_{11} - 0_{00}$ 1113 GHz lines, as well as the medium-*J* *p*-H₂O $2_{02} - 1_{11}$ at 988 GHz, $2_{11} - 2_{02}$ at 752 GHz, and the *o*-H₂O $3_{12} - 3_{03}$ 1097 GHz lines, together with at least one H₂¹⁸O, OH, and CO line (see Table 2). Several lines of ¹³CO, C¹⁸O, and hydrides are covered serendipitously in the same settings. Higher-*J* H₂O, OH, [O I], and CO lines are probed with a series of PACS settings on all low- and intermediate-mass sources, which provide 5×5 pixel minimaps on a $47'' \times 47''$ scale with $9.4''$ spacing to probe extended emission. The PACS data also give information on the dust continuum emission at wavelengths that have been poorly sampled to date. For high-mass YSOs and a few bright low-mass YSOs, full PACS spectral scans are taken, which cover many high-excitation H₂O lines in an unbiased way. Integration times are generally such that H₂O abundances down to $\sim 10^{-9}$ – 10^{-10} are probed, so that regions with significant freeze-out can be studied. Typically, 5–6 hr are spent per source to cover all lines, with integration times per line ranging from 10 minutes to 1 hr. For the prestellar cores and protoplanetary disks, long integration times with HIFI of up to 12 hr line⁻¹ are chosen to ensure that any nondetections are significant. These are the deepest observations carried out with HIFI across all KPs.

3.2. Observations and Data Reduction

3.2.1. HIFI

The bulk of the HIFI data are taken in dual-beam switch mode with a nod of $3'$ using fast chopping. The HIFI receivers are double-sideband with a sideband ratio close to unity. For

TABLE 1
WISH SOURCE LIST

Coordinates				Properties		Outflow ^a ('')	RD ^b	Ref.	Notes
R.A. (h m s)	Decl. (° ' ")	V_{LSR} (km s ⁻¹)	L_{bol} (L_{\odot})	d (pc)					
Prestellar Cores									
L 1544	05 04 17.2	+25 10 42.8	+7.3	...	140	
B 68	17 22 38.2	-23 49 54.0	+3.4	...	125	
Low-Mass YSOs									
L 1448-MM	03 25 38.9	+30 44 05.4	+5.3	11.6	250	R (+30, -125.4), B (-15, +28.8)	...	1, 2, 3	c
NGC1333 IRAS 2	03 28 55.6	+31 14 37.1	+7.7	20.7	235	B (-92, +28), R (+70, -15)	+	4, 2, 3	
NGC1333 IRAS 3A	03 29 03.8	+31 16 04.0	+8.5	50	235	B1 (+20, -20), B2 (+20, -50)	...	1, 5, 3	
NGC1333 IRAS 4A	03 29 10.5	+31 13 30.9	+7.2	7.7	235	B (-6, -19), R (+13, +25)	+	1, 2, 3	
NGC1333 IRAS 4B	03 29 12.0	+31 13 08.1	+7.4	7.7	235	...	+	1, 2, 3	
L 1527	04 39 53.9	+26 03 09.8	+5.9	2	140	B (+40, +10)	...	1, 2, 6	
BHR71	12 01 36.3	-65 08 53.0	-4.4	10	200	B (+40, -100), R (-40, +140)	...	6, 7, 8	
L 483 MM	18 17 29.9	-04 39 39.5	+5.2	9	200	B (-40, 0)	...	1, 2, 6	
Ser SMM1	18 29 49.8	+01 15 20.5	+8.5	30	250 ^l	B1 (-15, +30)	+	9, 10, 11	
Ser SMM4	18 29 56.6	+01 13 15.1	+8.0	5.0	250 ^l	R (+30, -60)	...	9, 12, 11	
Ser SMM3	18 29 59.2	+01 14 00.3	+7.6	5.9	250 ^l	9, 12, 11	
L 723 MM	19 17 53.7	+19 12 20.0	+11.2	3	300	6, 13	
B335	19 37 00.9	+07 34 09.6	+8.4	3	250	B (+30, 0)	...	1, 2, 6	
L 1157	20 39 06.3	+68 02 15.8	+2.6	6	325	B2 (+35, -95), R (-30, +140)	...	1, 2, 6	
L 1489	04 04 43.0	+26 18 57.0	+7.2	3.7	140	...	+	14, 15, 6	d
L 1551 IRS 5	04 31 34.1	+18 08 05.0	+7.2	28	140	B (-255, -255), R (+150, +20)	...	16, 12, 6	
TMRI ^m	04 39 13.7	+25 53 21.0	+6.3	3.7	140	4, 12, 6	
TMC1A ^m	04 39 34.9	+25 41 45.0	+6.6	2.2	140	12, 6	
TMC1	04 41 12.4	+25 46 36.0	+5.2	0.7	140	12, 6	
HH46	08 25 43.9	-51 00 36.0	+5.2	12	450	B (-10, 0), R (-40, -20)	...	17, 18	
Ced110 IRS4	11 06 47.0	-77 22 32.4	+3.5	1	125	19, 1, 20	
IRAS 12496/DKCha	12 53 17.2	-77 07 10.6	+2.3	50	200	1, 20	
IRAS 15398/B228	15 43 01.3	-34 09 15.0	+5.1	1	130	1, 20	
GSS 30 IRS1	16 26 21.4	-24 23 04.0	+2.8	25	125	1, 4, 21	
Elias 29	16 27 09.4	-24 37 19.6	+5.0	36	125	1, 22, 21	
Oph IRS 63	16 31 35.6	-24 01 29.6	+2.8	1.6	125	1, 22, 21	
RNO 91	16 34 29.3	16 34 29.3	+5.0	11	125	23, 1, 21	
R CrA IRS 5	19 01 48.0	-36 57 21.6	+5.7	3	170	24, 1, 20	
HH 100	19 01 49.1	-36 58 16.0	+5.6	14	125	25, 1, 20	
Intermediate-Mass YSOs									
AFGL 490	03 27 38.4	+58 47 08.0	-13.5	2000	1000	26, 27, 28	
L1641 S3MMS1	05 39 55.9	-07 30 28.0	+5.3	70	465	29, 30	
NGC 2071	05 47 04.4	+00 21 49.0	+9.6	520	422	P0 (+32, +63), P5 (-128, -97)	...	31, 32, 30	
Vela IRS 17	08 46 34.7	-43 54 30.5	+3.9	715	700	33, 34, 35	

TABLE 1 (Continued)

	Coordinates		Properties			Outflow ^a ($''$)	RD ^b	Ref.	Notes
	R.A. (h m s)	Decl. ($^{\circ}$ $'$ $''$)	V_{LSR} (km s^{-1})	L_{bol} (L_{\odot})	d (pc)				
Vela IRS 19	08 48 48.5	-45 32 29.0	+12.2	776	700	33, 35	
NGC7129 FIRS 2	21 43 01.7	+66 03 23.6	-9.8	430	1250	B (+60, +60), R (+60, -60)	+	36, 37, 38	
HH211-mm	03 43 56.8	+32 00 50	+9.2	4	250	C (0, 0), B2 (+37, -15)	
IRAS 04166	04 19 42.6	+27 13 38	+6.7	0.4	140	B (+20, +35), R (-20, -35)	
VLA-1 HH1/2	05 36 22.8	-06 46 07	+8	50	450	450 B (+60, -80)	
HH212 MM1	05 43 51.4	-01 02 53	+1.6	15	460	C (0, 0), B (-15, -35)	
HH25MMS	05 46 07.3	-00 13 30	+10	6	400	C (0, 0), SiO (+36, -57)	
HH111 VLA1	05 51 46.3	+02 48 30	+8.5	25	460	C (0, 0), B1 (-170, +21)	
HH54B	12 55 50.3	-76 56 23	+2.4	1	180	C (0, 0)	
VLA1623	16 26 26.4	-24 24 30	+3.5	1	125	B1 (+30, -20), R2 (-65, +25)	
IRAS 16293	16 32 22.8	-24 28 36	+4.5	14	125	B (+75, -60), R (+75, +45)	
Ser S 68N	18 29 47.5	+01 16 51	+8.5	4	260	B (-12, +24), C (0, 0)	
Cep E MM	23 03 13.1	+61 42 26	-11.0	75	730	B (-10, -20)	
High-Mass YSOs									
G11.11-0.12-NH ₃ -P1	18 10 33.9	-19 21 48	+30.4	...	3600	39, 40	e
G11.11-0.12-SCUBA-P1	18 10 28.4	-19 22 29	+29.2	...	3600	40	
G28.34+0.06-NH ₃ -P3	18 42 46.4	-04 04 12	+80.2	...	4800	40	
G28.34+0.06-SCUBA-P2	18 42 52.4	-03 59 54	+78.5	...	4800	40	
IRAS05358+3543	05 39 13.1	+35 45 50	-17.6	6.3×10^3	1800	41	f
IRAS16272-4837	16 30 58.7	-48 43 55	-46.2	2.4×10^4	3400	42	
NGC6334-I	17 20 53.3	-35 47 00	-4.5	1.7×10^4	1700	...	+	43	
W43-MM1	18 47 47.0	-01 54 28	+98.8	2.3×10^4	5500	44	
DR21(OH)	20 39 00.8	+42 22 48	-4.5	1.7×10^4	1700	45, 46	
W3-IRS5	02 25 40.6	+62 05 51	-38.4	1.7×10^5	2200	47, 78, 49	
IRAS18089-1732	18 11 51.5	-17 31 29	+33.8	3.2×10^4	3600	50	
W33A	18 14 39.5	-17 52 00	+37.5	1.0×10^4	4000	51	
IRAS18151-1208	18 17 58	-12 07 27	+32.0	2.0×10^4	2900	52	
AFGL2591	20 29 24.9	+40 11 19.5	-5.5	5.8×10^4	1700	53	
G327-0.6	15 53 08.8	-54 37 01	-45.0	1.0×10^5	3000	54, 55	h
NGC6334-I(N)	17 20 55.2	-35 45 04	-7.7	1.1×10^5	1700	56	
G29.96-0.02	18 46 03.8	-02 39 22	+98.7	1.2×10^5	7400	57, 58	
G31.41+0.31	18 47 34.3	-01 12 46	+98.8	1.8×10^5	7900	59, 60, 61	
IRAS20126+4104	20 14 25.1	+41 13 32	-3.8	1.0×10^4	1700	50	
G5.89-0.39	18 00 30.4	-24 04 02	+10.0	2.5×10^4	2000	62, 63	i
G10.47+0.03	18 08 38.2	-19 51 50	+67.0	1.1×10^5	5800	64, 65, 57	
G34.26+0.15	18 53 18.6	+01 14 58	+57.2	2.8×10^5	3300	66, 65	
W51N-e1	19 23 43.8	+14 30 26	+59.5	$1 - 10 \times 10^5$	5500	62	
NGC7538-IRS1	23 13 45.3	+61 28 10	-57.4	2.0×10^5	2800	...	+	67, 68	

TABLE 1 (*Continued*)

	Coordinates		Properties		Outflow ^a ($''$)	RD ^b	Ref.	Notes
	R.A. (h m s)	Decl. ($^{\circ}$ ' $''$)	V_{LSR} (km s ⁻¹)	L_{bol} (L_{\odot})				
S140	22 19 18.2	+63 18 46.9	-7.1	10^4	
DM Tau	04:33:49.7	+18:10:10	6.1	0.25	j
LKCa15	04:39:17.8	+22:21:04	6.0	0.74	
MWC480	04:58:46.3	+29:50:37	5.0	11.5	
TW Hya	11:01:51.9	-34:42:17	3.0	0.25	
BP Tau	04:19:15.8	+29:06:27	6.0	0.9	k
GG Tau	04:32:30.3	+17:31:41	7.0	0.8, 0.7	
GM Aur	04:55:10.2	+30:21:58	5.0	0.7	
MWC758	05:30:27.5	+25:19:57	5.5	21.0	
T Cha	11:57:13.5	-79:21:32	5.0	0.4	
IM Lup	15:56:09.2	-37:56:06	4.5	1.7	
AS209	16:49:15.3	-14:22:07	6.6	0.7	
HD163296	17:56:21.3	-21:57:20	6.0	35.0	

^a Also part of the outflow subprogram and will be observed at the given offset coordinates.^b Also part of the radiation diagnostics subprogram.^c Low-mass class 0 YSOs.^d Low-mass class I YSOs.^e High-mass prestellar cores.^f MIR-quiet HMPOs.^g MIR-bright HMPOs^h Hot molecular cores.ⁱ UC H II regions.^j Gas-rich disks, deep sample.^k Gas-rich disks, shallow sample^l Using VLBA observations of a star thought to be associated with the Serpens cluster; Dzib et al. (2010) derive a distance of 415 pc.^m Coordinates used in WISH; the more accurate coordinates obtained from SMA observations are 04 39 13.9, +25 53 20.6 (TMR1) and 04 39 35.2, +25 41 44.4 (TMC1A) (Jørgensen et al. 2009).

References.—(1) Evans et al. 2009; (2) Jørgensen et al. 2007; (3) Hirota et al. 2008; (4) Jørgensen et al. 2009; (5) Bachiller et al. 1998; (6) André et al. 2000; (7) Chen et al. 2008; (8) Seidensticker & Schmidt-Kaler 1989; (9) Kristensen et al. 2010b; (10) van Kempen et al. 2009; (11) Pontoppidan et al. 2004; (12) Hogerheijde et al. 1999; (13) Jørgensen et al. 2002; (14) Hogerheijde et al. 1997; (15) Brinch et al. 2007; (16) Butler et al. 1991; (17) Velusamy et al. 2007; (18) Noriega-Crespo et al. 2004; (19) Froebrich 2005; (20) Knude & Hog 1998; (21) de Geus et al. 1990; (22) Lommen et al. 2008; (23) Chen et al. 2009; (24) Nisini et al. 2005; (25) Wilking et al. 1992; (26) Gullixson et al. 1983; (27) Mozurkewich et al. 1986; (28) Snell et al. 1984; (29) Stanké et al. 2000; (30) Wilson et al. 2005; (31) Johnstone et al. 2001; (32) Butler et al. 1990; (33) Liseau et al. 1992; (34) Giamini et al. 2005; (35) Slawson & Reed 1988; (36) Fuente et al. 2005a; (37) Eiroa et al. 1998; (38) Shevchenko & Yakubov 1989; (39) Carey et al. 1998; (40) Pillai et al. 2006b; (41) Beuther et al. 2002a; (42) Garay et al. 2002; (43) Beuther et al. 2008; (44) Motte et al. 2003; (45) Csengeri et al. 2011, in preparation; (46) Motte et al. 2007; (47) Rodón et al. 2008; (48) Hachisuka et al. 2006; (49) Ladd et al. 1993; (50) Sridharan et al. 2002; (51) van der Tak et al. 2000b; (52) Beuther et al. 2002b; (53) van der Tak et al. 2006; (54) Wyrowski et al. 2002; (55) Bronfman et al. 1996; (56) Sandell 2000; (57) Beuther et al. 2007; (58) Gibb et al. 2004a; (59) Beltrán et al. 2005; (60) Cesaroni et al. 1998; (61) Mueller et al. 2002; (62) Sollins et al. 2004; (63) Hunter et al. 2008; (64) Olmi et al. 1996; (65) Wyrowski 2010, private communication; (66) Mookerjee et al. 2007; (67) Sandell & Sievers 2004; (68) De Buizer & Minter 2005.

TABLE 2
WISH LINE LIST

Species	Transition	ν (GHz)	λ (μm)	E_u/k_B (K)	A (s^{-1})	Ref.
HIFI Lines						
H ₂ O	1 ₁₀ – 1 ₀₁	556.936	538.3	61	3.5(–3)	1
H ₂ O	2 ₂₁ – 2 ₁₂	1661.008	180.5	194.1	3.1(–2)	1
H ₂ O	2 ₁₂ – 1 ₀₁	1669.905	179.5	114.4	5.6(–2)	1
H ₂ O	1 ₁₁ – 0 ₀₀	1113.343	269.3	53.4	1.8(–2)	1
H ₂ O	2 ₀₂ – 1 ₁₁	987.927	303.5	100.8	5.8(–3)	1
H ₂ O	2 ₁₁ – 2 ₀₂	752.033	398.6	136.9	7.1(–3)	1
H ₂ O	3 ₁₂ – 3 ₀₃	1097.365	273.2	249.4	1.6(–2)	1
H ₂ O	3 ₁₂ – 3 ₂₁	1153.127	260	249.4	2.6(–3)	1
H ₂ ¹⁸ O	1 ₁₀ – 1 ₀₁	547.676	547.4	60.5	3.3(–3)	1
H ₂ ¹⁸ O	1 ₁₁ – 0 ₀₀	1101.698	272.1	52.9	1.8(–2)	1
H ₂ ¹⁸ O	2 ₀₂ – 1 ₁₁	994.675	301.4	100.6	6.0(–3)	1
H ₂ ¹⁸ O	3 ₁₂ – 3 ₀₃	1095.627	273.6	248.7	1.6(–2)	1
H ₂ ¹⁷ O	1 ₁₀ – 1 ₀₁	552.021	543.1	60.7	3.4(–3)	1
H ₂ ¹⁷ O	1 ₁₁ – 0 ₀₀	1107.167	270.8	53.1	1.8(–2)	1
OH ^a	$\Omega, J = 1/2, 3/2 - 1/2, 1/2$	1834.747	163.4	269.8	6.4(–2)	1
OH ^a	$\Omega, J = 1/2, 3/2 - 1/2, 1/2$	1837.817	163.1	270.1	6.4(–2)	1
OH ⁺ a	$N_{J,F} = 1_{1,3/2} - 0_{1,3/2}$	1033.119	290.2	49.6	1.8(–2)	2
OH ⁺ a	$N_{J,F} = 2_{1,3/2} - 1_{1,3/2}$	1892.227	158.4	140.4	5.9(–2)	2
H ₂ O ⁺ a	$N_{K_a K_b, J} = 2_{02,3/2} - 1_{11,3/2}$	746.3	401.7	89.3	5.5(–4)	3
H ₂ O ⁺ a	$N_{K_a K_b, J} = 1_{11,3/2} - 0_{00,1/2}$	1115.204	268.8	53.5	3.1(–2)	6
H ₂ O ⁺ a	$N_{K_a K_b, J} = 1_{11,1/2} - 0_{00,1/2}$	1139.6	263.1	54.7	2.9(–2)	3
H ₂ O ⁺ a	$N_{K_a K_b, J} = 3_{12,5/2} - 3_{03,5/2}$	999.8	299.8	223.9	2.3(–2)	3
H ₃ O ⁺	$J_{k,+} = 0_{0,-} - 1_{0,+}$	984.712	304.4	54.7	2.3(–2)	1
H ₃ O ⁺	$J_{k,+} = 4_{3,+} - 3_{3,-}$	1031.294	290.7	232.2	5.1(–3)	1
H ₃ O ⁺	$J_{k,+} = 4_{2,+} - 3_{2,-}$	1069.827	280.2	268.8	9.8(–3)	1
H ₃ O ⁺	$J_{k,+} = 6_{2,-} - 6_{2,+}$	1454.563	206.1	692.6	7.1(–3)	1
H ₃ O ⁺	$J_{k,+} = 2_{1,-} - 2_{1,+}$	1632.091	183.7	143.1	1.7(–2)	1
CO	10–9	1151.985	260.2	304.2	1.0(–4)	1
CO	16–15	1841.346	162.8	751.7	4.1(–4)	1
¹³ CO	5–4	550.926	544.2	79.3	1.1(–5)	1
¹³ CO	10–9	1101.35	272.2	290.8	8.8(–5)	1
C ¹⁸ O	5–4	548.831	546.2	79	1.1(–5)	1
C ¹⁸ O	9–8	987.56	303.6	237	6.4(–5)	1
C ¹⁸ O	10–9	1097.163	273.2	289.7	8.8(–5)	1
HCO ⁺	6–5	535.062	560.3	89.9	1.3(–2)	1
CH ^a	$J_{F,P} = 3/2_{2,-} - 1/2_{1,+}$	536.761	558.5	25.8	6.4(–4)	2
CH ^a	$J_{F,P} = 5/2_{3,+} - 3/2_{2,-}$	1661.107	180.5	105.5	3.8(–2)	2
CH ^a	$J_{F,P} = 5/2_{3,-} - 3/2_{2,+}$	1656.956	180.9	105.2	3.7(–2)	2
CH ⁺	1–0	835.138	359	40.1	6.4(–2)	2
CH ⁺	2–1	1669.281	179.6	120.2	6.1(–2)	2
HCN	11–10	974.487	316.4	280.7	4.6(–2)	1
NH ^a	$N_{J,F,1,F} = 1_{2,5/2,7/2} - 0_{1,3/2,5/2}$	974.478	307.6	46.8	6.9(–3)	2
NH ^a	$N_{J,F,1,F} = 1_{1,3/2,5/2} - 0_{1,3/2,5/2}$	999.973	299.8	48	5.2(–3)	2
NH ⁺ a	$J_P = 3/2_- - 1/2_+$	1012.54	296.1	48.6	5.4(–2)	7

TABLE 2 (Continued)

Species	Transition	ν (GHz)	λ (μ m)	E_u/k_B (K)	A (s^{-1})	Ref.
NH ⁺ ^a	$J_P = 3/2_+ - 1/2_-$	1019.211	294.1	48.9	5.5(-2)	7
NH ₃	$1_0 - 0_0$	572.498	523.7	27.5	1.6(-3)	1
C ⁺	$2P_{3/2} - 2P_{1/2}$	1900.537	157.7	91.3	2.3(-6)	5
SH ⁺ ^a	$N_{J,F} = 2_{3,7/2} - 1_{2,5/2}$	1082.912	276.8	77.2	9.8(-3)	2
SH ⁺ ^a	$N_{J,F} = 3_{4,9/2} - 2_{3,5/2}$	1632.518	183.6	155.6	3.6(-2)	2
SH ⁺ ^a	$N_{J,F} = 1_{2,5/2} - 0_{1,3/2}$	526.048	569.9	25.2	9.6(-4)	2
CS	11-10	538.689	556.5	155.1	3.3(-3)	1
SH ^a	$N'_\Lambda = 3_{+1} - 2_{-1}$	1447.012	207.2	640.6	8.1(-3)	1
PACS Lines						
H ₂ O	$2_{21} - 2_{12}$	1661.008	180.5	194.1	3.1(-2)	1
H ₂ O	$2_{12} - 1_{01}$	1669.905	179.5	114.4	5.6(-2)	1
H ₂ O	$3_{03} - 2_{12}$	1716.77	174.6	196.8	5.1(-2)	1
H ₂ O	$3_{13} - 2_{02}$	2164.132	138.5	204.7	1.3(-1)	1
H ₂ O	$3_{30} - 3_{21}$	2196.346	136.5	410.7	6.6(-2)	1
H ₂ O	$4_{04} - 3_{13}$	2391.573	125.4	319.5	1.7(-1)	1
H ₂ O	$4_{14} - 3_{03}$	2640.474	113.5	323.5	2.5(-1)	1
H ₂ O	$2_{21} - 1_{10}$	2773.977	108.1	194.1	2.6(-1)	1
H ₂ O	$3_{22} - 2_{11}$	3331.458	90	296.8	3.5(-1)	1
H ₂ O	$7_{07} - 6_{16}$	4166.852	71.9	843.5	1.2(0)	1
H ₂ O	$8_{18} - 7_{07}$	4734.296	63.3	1070.7	1.8(0)	1
H ₂ O	$9_{09} - 8_{18}$	5276.52	56.8	1323.9	2.5(0)	1
OH	$\Omega, j = \frac{1}{2} - \frac{1}{2}$	1834.747	163.4	269.8	6.4(-2)	1
OH	$\Omega, j = \frac{3}{2} - \frac{3}{2}$	1837.817	163.1	270.1	6.4(-2)	1
OH	$\Omega, j = \frac{1}{2} - \frac{1}{2}$	2509.949	119.4	120.5	1.4(-1)	1
OH	$\Omega, j = \frac{3}{2} - \frac{3}{2}$	2514.317	119.2	120.7	1.4(-1)	1
OH	$\Omega, j = \frac{1}{2} - \frac{1}{2}$	3543.779	84.6	290.5	5.1(-1)	1
OH	$\Omega, j = \frac{3}{2} - \frac{3}{2}$	3551.185	84.4	291.2	5.2(-1)	1
OH	$\Omega, j = \frac{1}{2} - \frac{1}{2}$	3786.17	79.2	181.7	3.5(-2)	1
OH	$\Omega, j = \frac{3}{2} - \frac{3}{2}$	3789.18	79.1	181.9	3.5(-2)	1
CO	$14-13$	1611.794	186	580.5	2.7(-4)	1
CO	$16-15$	1841.346	162.8	751.7	4.1(-4)	1
CO	$18-17$	2070.616	144.8	945	5.7(-4)	1
CO	$22-21$	2528.172	118.6	1397.4	1.0(-3)	1
CO	$23-22$	2642.33	113.5	1524.2	1.1(-3)	1
CO	$24-23$	2756.388	108.8	1656.5	1.3(-3)	1
CO	$29-28$	3325.005	90.2	2399.8	2.1(-3)	1
CO	$30-29$	3438.365	87.2	2564.8	2.3(-3)	1
CO	$31-30$	3551.592	84.4	2735.3	2.5(-3)	1
CO	$32-31$	3664.684	81.8	2911.2	2.7(-3)	1
CO	$33-32$	3777.634	79.4	3092.5	3.0(-3)	1
CO	$36-35$	4115.606	72.8	3668.8	3.6(-3)	1
O	$^3P_1 - ^3P_2$	4166.852	63.2	227.7	8.9(-5)	5
O	$^3P_0 - ^3P_1$	5276.519	145.5	326.6	1.8(-5)	5
C ⁺	$2P_{3/2} - 2P_{1/2}$	1900.537	157.7	91.3	2.3(-6)	5

^a Fine/hyperfine-structure transition. Only the strongest component is listed here.**References.**—(1) Pickett et al. 1998; (2) Müller et al. 2001; (3) Bruderer 2006; (4) Bruderer et al. 2010b; (5) Ralchenko et al. 2008; (6) Mürtz et al. 1998; (7) Hübers et al. 2009.

line-rich sources (mostly high-mass YSOs), the local oscillator was shifted slightly for half of the integration time to disentangle lines from the upper and lower sidebands. Two polarizations, H and V , are measured simultaneously and are generally averaged together to improve the signal-to-noise ratio (S/N). In some cases, differences of the order of 30% are found between the two polarizations, in which case only the higher-quality H -band spectra are used for analysis, since the mixers have been optimized for the H band. Two back ends are employed: the low-resolution back end (wideband spectrometer [WBS]) with an instantaneous bandwidth of 4 GHz at 1.1 MHz spectral resolution (~ 1100 and 0.3 km s^{-1} at 1 THz, respectively) and the high-resolution back end (high-resolution spectrometer [HRS]) with a variable bandwidth and resolution (typically 230 MHz bandwidth and 250 kHz resolution, or ~ 63 and 0.07 km s^{-1} at 1 THz, respectively).

Data reduction of the HIFI spectra involves the usual steps of checking individual exposures for bad spectra, summing exposures, taking out any baseline ripples, fitting a low-order polynomial baseline, and making Gaussian fits or integrating line intensities, as appropriate. The data are reduced within the *Herschel* interactive processing environment (HIPE) (Ott 2010) and can be exported to CLASS⁴⁹ after level 2 for further analysis. The main-beam efficiency has been determined to be around 0.76, virtually independent of frequency, except for a 15% lower value at around 1.1–1.2 THz (Olberg 2010), and the absolute calibration is currently estimated to be better than $\sim 15\%$ for HIFI bands 1, 2, and 5 and $\sim 30\%$ for bands 3, 4, 6, and 7. The rms noise in the WBS data is generally lower than that in the HRS data by a factor of 1.4 when binned to the same spectral resolution, due to a $\sqrt{2}$ loss factor in the HRS autocorrelator.

3.2.2. PACS

PACS is a 5×5 array of $9.4'' \times 9.4''$ spaxels (spatial pixels) with very small gaps between the pixels. Each spaxel covers the 53–210 μm wavelength range, with a spectral resolving power ranging from 1000 to 4000 (the latter only below 63 μm) in spectroscopy mode. In one exposure, a wavelength segment is observed in the first order (105–210 μm) and at the same time in the second (72–105 μm) or third order (53–72 μm). Two different nod positions, located $6'$ in opposite directions from the target, are used to correct for telescopic background. Data are reduced within HIPE. The uncertainty in absolute and relative fluxes is estimated to be about 10–20%, based on comparison with the *ISO-LWS* data.

The diffraction-limited beam is smaller than a spaxel of $9.4''$ at wavelengths shortward of 110 μm . At longer wavelengths, the point-spread function (PSF) becomes significantly larger, such that at 200 μm only 40% of the light of a well-centered

point source falls on the central pixel. Even at 100 μm , 30% of the light still falls outside the central spaxel. Thus, observed fluxes reported for a single pixel have to be corrected for the point-source PSF using values provided by the Herschel Science Center. For extended sources, fluxes can be summed over the spaxels to obtain the total flux. In case of a bright central source with extended emission, such as along an outflow, fluxes at the outflow positions were corrected for the leaking of light from the central spaxel into adjacent spaxels.

3.3. Archival Value

All reduced HIFI and PACS spectra will be delivered to the Herschel Science Center approximately one year after the last KP data have been taken, assuming that reliable calibration is available in a timely manner. The delivery will consist of reduced and calibrated HIFI spectra, line profile parameters (either Gaussian fits or integrated intensities, depending on line), and reduced small maps, most likely in FITS format. A quick-look spectral browser will be on the team Web site. For PACS, a data cube of calibrated images will be delivered, similar to that for integral field spectrometers.

Over the past decade, the WISH team has collected a wealth of complementary data on various molecular lines for the majority of our sources using the JCMT, IRAM 30 m, APEX, CSO, Onsala, and other single-dish telescopes. These data include tracers of the cloud velocity structure and column density (^{12}CO , ^{13}CO , C^{18}O $J = 1-0$, $2-1$, and $3-2$, probing ~ 30 K gas), high-temperature lines (CO and isotopologs 6–5, 7–6, probing ~ 50 –100 K gas), and high-density tracers (CS and C^{34}S $2-1$, $5-4$, $7-6$; HCO^+ and H^{13}CO^+ $3-2$, $4-3$, probing $n > 10^5 \text{ cm}^{-3}$), as well as the atomic [C I] line (probing UV radiation). Moreover, grain surface chemistry products are observed through various H_2CO and CH_3OH lines, whereas shocks powerful enough to disrupt grain cores are traced through SiO emission. Examples of such studies are van der Tak et al. (2000b), Jørgensen et al. (2004), Fuente et al. (2005b), Nisini et al. (2007), and Marseille et al. (2008).

A recent development is the use of heterodyne array receivers such as the 9 pixel HERA 230 GHz array at the IRAM 30 m, the HARP-B 16 pixel 345 GHz receiver at the JCMT (e.g., van Kempen et al. 2009b; Kristensen et al. 2010a), and the dual-frequency 2×7 pixel CHAMP + 650/850 GHz receiver at APEX (e.g., van Kempen et al. 2009d, 2009e). The spatial resolution of these telescopes is typically 7–15": i.e., comparable with that of *Herschel* at the higher frequencies. These data also provide an image of the warm dense gas contained within the $\sim 37''$ *Herschel* beam at 557 GHz. Millimeter interferometry data down to $\sim 1''$ resolution also exist for a significant subset of the sources in various molecules and lines (e.g., Fuente et al. 2005a; van der Tak et al. 2006; Benz et al. 2007; Jørgensen et al. 2009; and references therein). Except for the compact hot core, however, such data cannot be compared directly with single-dish

⁴⁹ See <http://iram.fr/IRAMFR/GILDAS>.

data from *Herschel*, since a significant fraction of the extended emission is resolved out in the interferometer.

Finally, submillimeter continuum maps obtained with JCMT-SCUBA, IRAM-MAMBO, and/or APEX-LABOCA are available at 10–20" resolution for most embedded sources (e.g., Di Francesco et al. 2008), as are ground-based and mid-IR *Spitzer* observations of ices (Gibb et al. 2004b; Boogert et al. 2008). *Spitzer* infrared spectrograph mid-infrared H₂ maps have been taken for the three outflow targets studied in detail (Neufeld et al. 2009).

The ground-based complementary data will be summarized in a table at the KP Web site. For several subprograms, the most relevant data will be available directly at the KP Web site. Specifically, in collaboration with the DIGIT KP, a searchable Web-based archive of complementary submillimeter single-dish, interferometer, and infrared spectra is being built for low-mass YSOs.

4. RESULTS

In the following, a brief description of the scientific motivation and observing strategy for each of the subprograms is given, together with initial results. Full source and line lists are given in Tables 1 and 2. Unless otherwise specified, the cited noise limits are for 0.2–0.4 km s^{−1} velocity bins, and all stated results refer to main-beam antenna temperatures, T_{MB} .

4.1. Prestellar Cores

4.1.1. Motivation

In recent years, a number of cold, highly extincted clouds have been identified that have a clear central density condensation (see the overview by Bergin & Tafalla 2007). Several of these so-called prestellar cores are thought to be on the verge of collapse and thus represent the earliest stage in the star-formation process (e.g., Tafalla et al. 1998; Caselli et al. 2002; Crapsi et al. 2005). It is now widely accepted that most molecules are highly depleted in the inner dense parts of these cores (e.g., Caselli et al. 1999; Bergin et al. 2002; Tafalla et al. 2006). H₂O should be no exception, although its formation as an ice already starts in the general molecular cloud phase. The physical properties of these cores are very well constrained from ground-based continuum and line data and they are the most pristine types of clouds, without any internal heat sources and almost no turbulence. Thus, they form the best laboratories to test chemical models. Since H₂O is the dominant ice component and has a very different binding energy and formation route than CO, HIFI observations of H₂O will form a critical benchmark to test gas-grain processes.

HIFI will be key to address the questions: (1) Where does the onset of H₂O ice formation and freeze-out occur in dense prestellar cores? (2) How effective are nonthermal desorption mechanisms (photodesorption at edge, cosmic-ray-induced desorption in center) in maintaining some fraction of O and H₂O

in the gas phase? (3) Is the H₂O abundance in the gas phase sensitive to the prestellar core environment?

4.1.2. Source and Line Selection

Two well-studied prestellar cores, B68 and L1544, are observed in the *o*-H₂O 557 GHz line at the central position down to ~2 mK rms. Both are at $d < 200$ pc and have bright millimeter dust continuum emission, a simple morphology, and centrally concentrated density profiles. B68 is an isolated dark globule exposed to the general interstellar radiation field, whereas L1544 is a dense core embedded in a larger cloud. The sensitivity limits are based on H₂O column densities estimated using the model results of Aikawa et al. (2005) for chemically “old” sources like L1544. From the predicted abundance profile and the density structure, column densities have been determined at different impact parameters and convolved with the HIFI beam at 557 GHz. The brightness temperatures have been derived using the non-LTE radiative transfer codes of Hogerheijde & van der Tak (2000) and Keto et al. (2004). The results are very sensitive to the temperature structure of the core, the initial H₂O abundance in the chemical models, and the assumed ortho/para ratio of both H₂O and H₂. Pre-*Herschel* model predictions ranged from peak antenna temperatures of below 10 mK (Hollenbach et al. 2009) to several hundred degrees milliKelvin.

4.1.3. Initial Results

Caselli et al. (2010) present early results for the two cores, with the B68 *o*-H₂O 1₁₀ – 1₀₁ spectrum included in Figure 4. These spectra took ~4 hr integration (on + off) each. No emission line is detected in B68 down to 2.0 mK rms in 0.6 km s^{−1} bins. This is more than an order of magnitude lower than the previous upper limit obtained by *SWAS* for this cloud (Bergin & Snell 2002), as well as by most pre-*Herschel* model predictions. The 3 σ upper limit corresponds to an *o*-H₂O column density $< 2.5 \times 10^{13}$ cm^{−2} and a mean line-of-sight abundance of $< 1.3 \times 10^{-9}$. This is consistent with the nondetection predicted by the model of Hollenbach et al. (2009) applied to B68.

Interestingly, the L1544 spectrum shows a tentative *absorption* feature against the submillimeter continuum, which closely matches the velocity range spanned by the CO 1–0 emission line. If the water absorption is confirmed by deeper integrations, which are currently planned within WISH, it provides a very powerful tool to determine the water abundance profile along the line of sight.

Initial radiative transfer analyses, based on the Keto & Caselli (2010) models, imply an H₂O abundance profile for both clouds that peaks at an abundance of $\sim 10^{-8}$ in the outer region of the core, where the density is too low for significant freeze-out, but where the gas is sufficiently shielded from photodissociation ($A_V > 2$ mag). The abundance drops by more than an order of magnitude in the central part, due to freeze-out. These new

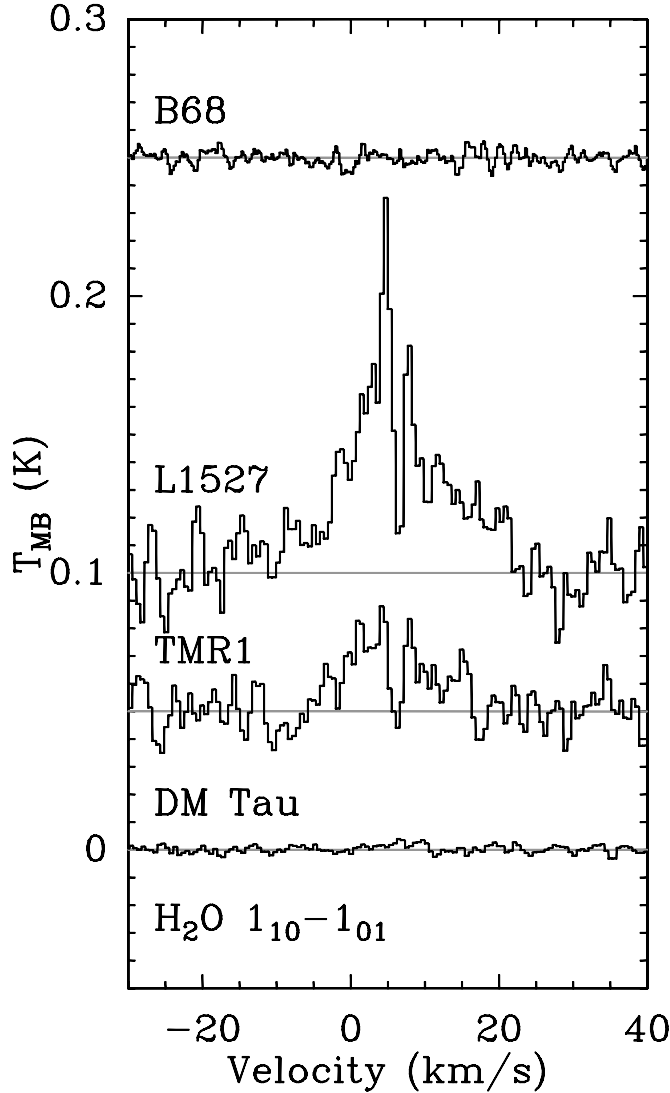


FIG. 4.—HIFI spectra of the o -H₂O $1_{10} - 1_{01}$ 557 GHz line. From top to bottom: the prestellar core B68 (Caselli et al. 2010), the low-mass stage 0 YSO L1527, the low-mass stage 1 YSO TMR-1, and the protoplanetary disk DM Tau (Bergin et al. 2010b). See the electronic edition of the *PASP* for a color version of this figure.

predictions are based on an improved physical structure of the L1544 core and on an H₂O abundance profile that includes the freeze-out, a generalized desorption from Roberts & Millar (2007), and photodissociation, but no detailed gas phase and surface chemistry. Such abundance profiles differ from those expected from chemical models by Aikawa et al. (2005), who predict higher H₂O abundances toward the core center and thus brighter lines. Investigations are currently underway to understand which processes are producing the different abundance structures.

These results demonstrate that questions 1 and 2 in § 4.1.1 can be addressed by the *Herschel* observations, provided the

integrations are deep enough. Question 3 requires observations of a larger sample of cores than those studied in WISH.

4.2. Low-Mass Young Stellar Objects

4.2.1. Motivation

Once the cloud has started to collapse and a protostellar object has formed, the envelope is heated from the inside by the accretion luminosity. The physical structure of these low-mass deeply embedded objects ($\lesssim 100 L_{\odot}$) is complex, with large gradients in temperature and density in the envelope, a compact disk at the center, and stellar jets and winds creating a cavity in the envelope and affecting the surrounding material (e.g., van Dishoeck et al. 1995; Jørgensen et al. 2005a; Chandler et al. 2005) (see Fig. 5). The high spatial and spectral resolutions at far-infrared wavelengths offered by *Herschel* are key to disentangling these processes.

Several evolutionary stages can be distinguished for low-mass YSOs (see the nomenclature by Robitaille et al. 2006). In the earliest deeply embedded stage 0, the main accretion phase, the envelope mass is still much larger than that of the protostar or disk ($M_{\text{env}} \gg M_{*}$ and $\gg M_{\text{disk}}$). At the subsequent stage 1, the star is largely assembled and now has a much larger mass than the disk ($M_{*} \gg M_{\text{disk}}$), but the envelope still dominates the circumstellar material ($M_{\text{env}} > M_{\text{disk}}$). At stage 2, the envelope has completely dissipated and only a gas-rich disk is left around the young pre-main-sequence star. Observationally, low-mass YSOs are usually classified based on their spectral energy distributions according to their spectral slopes (as in the Lada classes) or bolometric temperatures (see the summary in Evans et al. 2009). The classes 0 and II sources generally correspond well to the evolutionary stages 0 and 2 cases. In contrast, the traditional class I sources are found to be a mix of true stage 1 sources and of stage 2 disks, which are either seen edge-on or which have a large amount of foreground extinction, resulting in a rising infrared spectrum (see the discussion in Crapsi et al. 2008).

ISO-LWS observations have shown that low-mass YSOs are copious water emitters, with more than 70% of the stage 0 sources detected in H₂O lines with energies up to 500 K above ground (see the summary by Nisini et al. 2002). Two scenarios have been put forward to explain these strong lines. In one model, the lines arise primarily from the bulk of the envelope, with the lower-energy lines originating in the outer envelope and the higher-energy lines originating from the inner hot core (Maret et al. 2002). In the alternative interpretation, most of the H₂O emission is associated with the outflows impacting the surrounding gas on larger scales (e.g., Giannini et al. 2001).

In contrast, none of the low-mass stage 1 sources show H₂O lines in the *ISO-LWS* beam (Giannini et al. 2001). Possible explanations given in that article include dissociation resulting from enhanced penetration of X-rays or UV photons or a longer timescale enhancing freeze-out. HIFI can distinguish between

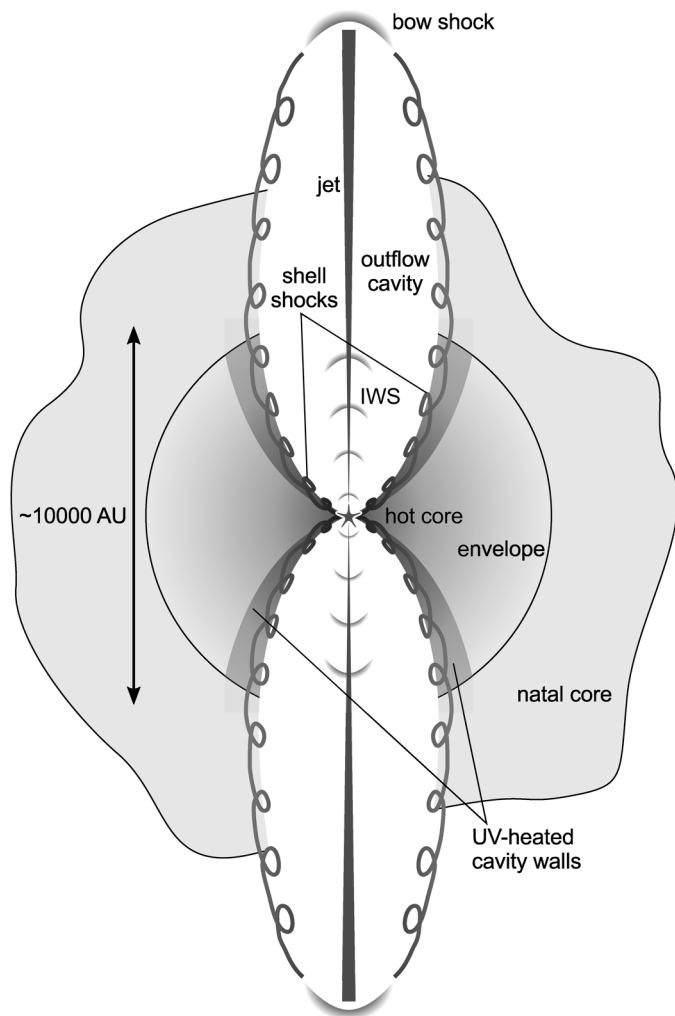


FIG. 5.—Illustration of a protostellar envelope with the different physical components and their nomenclature indicated. IWS stands for internal working surfaces. The indicated scale is appropriate for a low-mass YSO (Visser et al. 2011, in preparation). On this scale, the ~ 100 AU radius disk surrounding the protostar is not visible. See the electronic edition of the *PASP* for a color version of this figure.

the different scenarios by providing much deeper searches than *ISO-LWS*, as well as the photodissociation products OH and O, and X-ray products such as ions. Indeed, OH/ H_2O abundance ratios are expected to change by factors of >100 due to UV and X-rays (Stäuber et al. 2006). Complementary infrared data on H_2O ice are available for many of these sources so that the gas/ice ratio can be measured directly.

Key questions to be addressed are as follows: (1) What is the origin of the strong H_2O emission in low-mass stage 0 protostars: passively heated envelope or shocked outflow material? What is the role of the outflow cavity? (2) Is the high water abundance governed by high-temperature chemistry or grain mantle evaporation? (3) Do low-mass stage 1 sources indeed have much lower H_2O abundances? If so, is this due to en-

hanced UV, X-rays, or other effects such as lower outflow activity? (4) What is the $\text{HDO}/\text{H}_2\text{O}$ ratio in the protostellar phase, and what does this tell us about the efficiency of grain surface deuteration? How does $\text{HDO}/\text{H}_2\text{O}$ evolve during star formation? Is it similar to that found in comets?

4.2.2. Source and Line Selection

A set of 14 deeply embedded stage 0 sources has been selected from the list of André et al. (2000) and 15 stage 1 sources have been selected from the lists of Tamura et al. (1991) and André & Montmerle (1994) and from the spectroscopic part of the *Spitzer* Cores to Disks legacy program (Evans et al. 2003, 2009). All sources have $d < 450$ pc and are well characterized with a variety of other single-dish submillimeter telescopes and interferometers (Jørgensen et al. 2004, 2007). In particular, only bona fide stage 1 embedded YSOs are included, with the stage verified through complementary single-dish and interferometer data (van Kempen et al. 2009b; Jørgensen et al. 2009).

The line selection for the stage 0 sources follows the general philosophy outlined in § 3.1, with typical integration times for the HIFI lines such that 20–100 mK rms is reached in $\sim 0.5 \text{ km s}^{-1}$ bins, depending on the line, and down to 5 mK for H_2^{18}O . For reference, observed widths of molecular lines originating in the bulk of the envelopes are typically 1–2 km s^{-1} FWHM. The noise limits are based on 1D envelope models by van Kempen et al. (2008) for L483, one of the weaker stage 0 sources, and do not include any outflow contribution. Not all lines are observed for all sources: some time-consuming higher-frequency lines are dropped for the weaker ones. Selected PACS lines are observed to cover the higher-excitation emission and obtain information on the spatial extent. Full PACS spectral scans are made of four stage 0 sources (NGC 1333 IRAS 4A/B, IRAS2A, and Serpens SMM1) to obtain an unbiased view of the higher- H_2O lines. For the stage 1 objects, only four H_2O lines and one CO line are observed with HIFI. The set of PACS lines observed for these sources is also more limited.

4.2.3. Initial Results

Figure 6 presents spectra of the lowest two $p\text{-H}_2\text{O}$ lines toward one of the brightest low-mass stage 0 sources, NGC 1333 IRAS2A (Kristensen et al. 2010b), and Fig. 4 includes the lowest $o\text{-H}_2\text{O}$ line toward the stage 0 source L1527. The profiles are surprisingly broad and complex. They can be decomposed into three components: broad ($>20 \text{ km s}^{-1}$), medium-broad ($\sim 5\text{--}10 \text{ km s}^{-1}$), and narrow ($2\text{--}3 \text{ km s}^{-1}$) components, with the latter seen primarily in (self-)absorption in the ground-state transitions. The central velocities of the three components can vary relative to each other from source to source, probably due to different viewing angles and geometries of the systems. For one stage 0 source, NGC 1333 IRAS4A, the $2_{02} - 1_{11}$ line shows an inverse P-Cygni profile that is indicative of large-scale

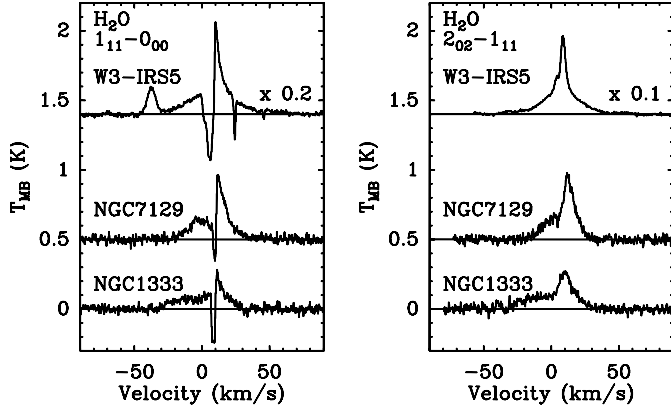


FIG. 6.—HIFI spectra of the p -H₂O $1_{11} - 0_{00}$ 1113 GHz (left) and $2_{02} - 1_{11}$ 988 GHz (right) lines. From top to bottom: the high-mass YSO W3 IRS5 ($L = 1.5 \times 10^5 L_{\odot}$ and $d = 2.0$ kpc) (Chavarría et al. 2010), the intermediate-mass YSO NGC 7129 FIRS2 (430 L_{\odot} and 1260 pc) (Johnstone et al. 2010), and the low-mass YSO NGC 1333 IRAS2A (20 L_{\odot} and 235 pc) (Kristensen et al. 2010b). All spectra have been shifted to a central velocity of 0 km s⁻¹. The redshifted absorption features seen in the $1_{11} - 0_{00}$ spectrum toward W3 IRS5 are due to water in foreground clouds, whereas the small emission line on the blue-shifted side can be ascribed to the SO₂ $13_{9,5} - 12_{8,4}$ transition.

infall. Interestingly, the H₂¹⁸O lines only reveal the broad component.

From the profiles themselves, it can be concluded immediately that the bulk of the water emission arises from shocked gas and not in the quiescent envelope; a hot-core region with an enhanced H₂O abundance and an infall velocity profile gives lines with widths of, at most, 4–5 km s⁻¹ (Visser et al. 2011, in preparation). The broad component is associated with shocks on large scales along the outflow cavity walls, as traditionally probed with the standard high-velocity CO outflows (labeled as shell shocks in Fig. 5). The medium component is linked to shocks on smaller scales in the dense inner envelope (<1000 AU), based on comparison of the line profiles with those of high-density tracers and with interferometer data (Kristensen et al. 2010b). The H₂O/CO abundance ratios in the shocks are high, ~ 0.1 – 1 , corresponding to H₂O abundances of $\sim 10^{-5}$ – 10^{-4} with respect to H₂. The highest abundances are found at the highest velocities, indicating that only a small percentage of the gas is processed at high-enough temperatures such that all O is driven into H₂O. This small percentage is consistent with the findings of Franklin et al. (2008) based on SWAS data.

The narrow water absorption lines probe the quiescent outer envelope and any foreground material. Together with the absence of narrow H₂¹⁸O $1_{10} - 1_{01}$ emission and the maximum narrow emission that can be hidden in the H₂O profiles, these lines constrain the H₂O abundance in the bulk of the cold envelope to $\sim 10^{-8}$. The lack of (narrow) H₂¹⁸O $2_{02} - 1_{11}$ emission down to ~ 10 mK rms limits the water abundance in the inner ice evaporation zone to $< 10^{-5}$ (Visser et al. 2011, in preparation). In contrast, the warm quiescent envelope with $T > 25$ K is clearly revealed by HIFI in narrow C¹⁸O 9–8 emission

lines, where the CO abundance jumps by a factor of at least a few (Yıldız et al. 2010).

Figure 4 includes the o -H₂O 557 GHz $1_{10} - 1_{01}$ HIFI spectrum of the stage 1 source TMR-1. This is the first detection of the H₂O 557 GHz line in this stage. The fact that the line is weaker than for the stage 0 source is consistent with the non-detection by ISO. Again, the broad line points to an origin in the outflow shocks, rather than the quiescent envelope.

The combination of ground-based, HIFI, and PACS data (Fig. 7) allows the complete CO ladder from $J = 2$ – 1 up to 43 – 42 to be characterized for a low-mass YSO for the first time (van Kempen et al. 2010b). Because CO is much less sensitive to chemical effects than H₂O, this provides an opportunity to test various gas heating processes. Figure 8 shows the CO excitation diagram for the stage 1 source HH 46, giving a rotational temperature of 410 ± 25 K. Also included in this figure are data for another WISH source, Serpens SMM1, for which a full PACS spectral scan has been obtained. The entire CO ladder can be fit by a single rotational temperature of 520 ± 20 K. CO ladders have also been published for two sources from the DIGIT first results, the stages 1–2 transitional source DK Cha and the disk around the Herbig star HD 100546 (van Kempen et al. 2010a; Sturm et al. 2010). In both cases, the data indicate excitation temperatures of several hundred degrees Kelvin, but with evidence for a two-temperature-component structure in at least one source. Such a two-component fit does not necessarily imply two different physical regimes or a temperature gradient, however. Optical depth effects in the CO lines can also lead to curvature in the rotational diagrams.

Because of the limited information that can be derived from an excitation diagram, a detailed model has been developed for HH 46 using the known physical structure of the quiescent envelope as a starting point (van Kempen et al. 2009d). The passively heated envelope can explain only the lowest CO rotational transitions, so additional heating mechanisms are needed (see Fig. 5). One possibility is UV photon heating, in which the UV photons produced in the immediate protostellar environment can escape through the cavity carved by the jet and wind from the young star and impinge on the envelope at much larger distances from the star (up to a few thousand AU). It is found that this UV heating of the outflow cavity walls can well reproduce the intermediate transitions up to $J < 20$, depending on the precise PDR model used. Another mechanism is necessary to populate the highest CO levels $J > 20$: small-scale shocks with velocities of ~ 20 km s⁻¹ pasted along the walls can explain these lines well (van Kempen et al. 2010b; Visser et al. 2011, in preparation). This model solution is not unique and is sensitive to model details, but it demonstrates that a good fit can be found with just two free parameters: the UV flux and the shock velocity.

Figure 7 presents maps of the CO, H₂O, and [O I] lines observed with PACS toward the isolated stage 1 source IRAS 15398–3359, known for its peculiar carbon chemistry (Sakai et al.

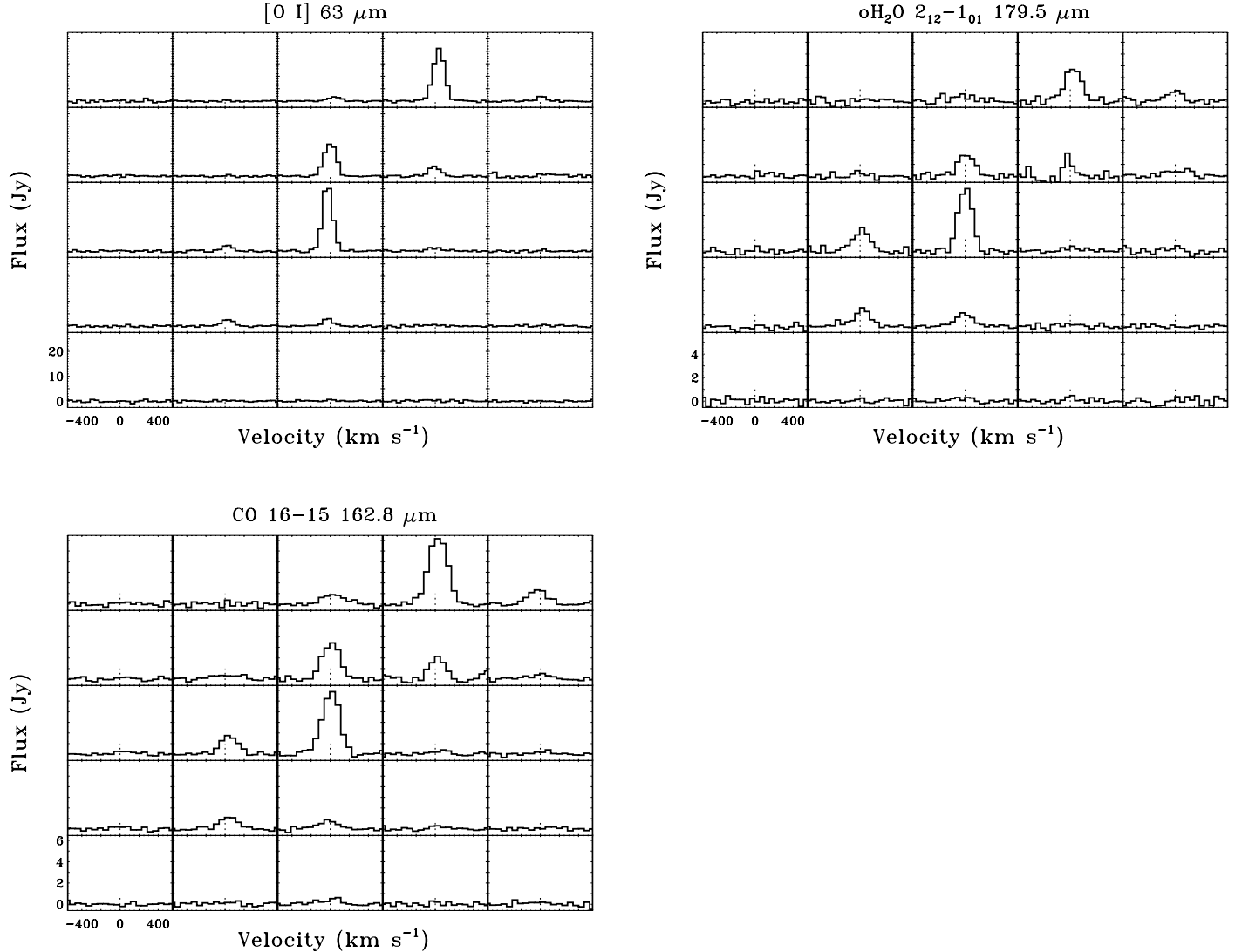


FIG. 7.—PACS 5×5 spectral maps of the $[\text{O I}]^3P_1 - ^3P_2$ $63 \mu\text{m}$ (left), $\text{H}_2\text{O } 2_{12} - 1_{01}$ $179 \mu\text{m}$ (middle) and $\text{CO } J = 16-15$ $163 \mu\text{m}$ lines (right) toward the low-mass stage 1 YSO IRAS 15398-3359. All lines are extended along the outflow direction seen in the low- J CO map of van Kempen et al. (2009a).

2009). All lines are clearly extended in the outflow direction as mapped in lower- J CO lines (van Kempen et al. 2009a), confirming their association with the shocks and outflow cavities.

The amount of cooling produced by each of the species can be quantified from the PACS data. In the central HH 46 spaxel, $[\text{O I}]$ and OH dominate the cooling (at least 60% of the total cooling in far-infrared lines), followed by H_2O ($\sim 30\%$) and CO ($\sim 10\%$). The total far-infrared line cooling of at least $2.4 \times 10^{-2} L_\odot$ is consistent with the kinetic luminosity found by van Kempen et al. (2009d) from CO outflow maps and follows the relation found by Giannini et al. (2001) between these two quantities. The $[\text{O I}]$ $63 \mu\text{m}$ line is spectrally resolved with PACS and reveals a jet component with velocities up to 170 km s^{-1} associated with the blue- and redshifted outflow seen in optical atomic lines

in less extinguished regions of the flow. This is the first time that such a jet has been seen in a far-infrared line, providing a powerful diagnostic of the “hidden jet” in the densest optically opaque regions. OH is detected strongly on source, but not along the outflow axis, in contrast with other species. Both the $[\text{O I}]$ and OH emissions are ascribed to a dissociative shock caused by the jet impacting on the inner dense ($> 10^6 \text{ cm}^{-3}$) envelope; disk emission is excluded by scaling the observed disk emission from stage 2 sources to the distance of HH 46 (van Kempen et al. 2010b). In dissociative shocks, OH is one of the first molecules to reform after molecular dissociation, whereas the UV radiation from the shock and the high H/H_2 ratio prevent effective H_2O formation in the postshock gas (Neufeld & Dalgarno 1989). Once H_2 is reformed, the heat of H_2 formation maintains a temperature

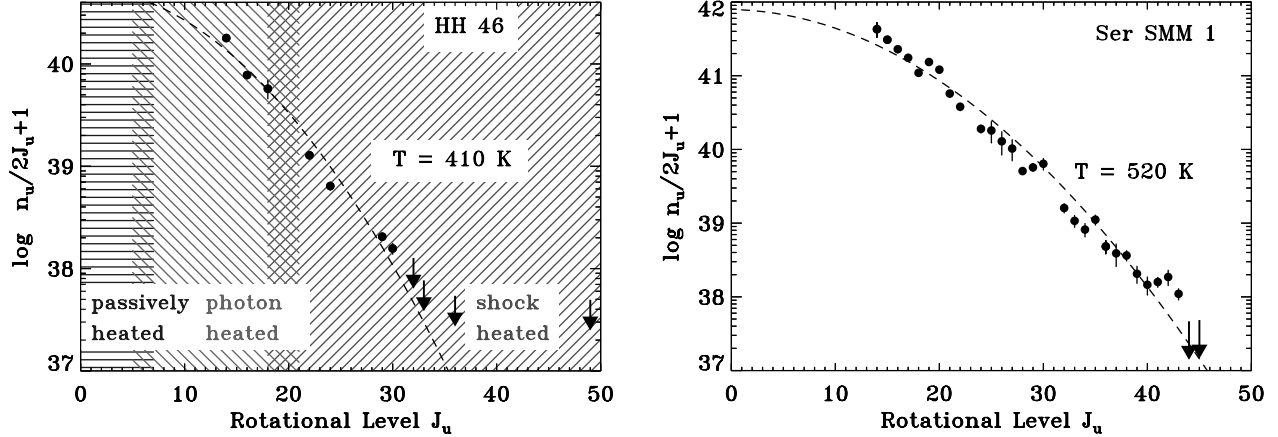


FIG. 8.—Diagram illustrating the CO excitation. The number of molecules in the upper level divided by its statistical weight is plotted versus rotational quantum number J_u . *Left*: Low-mass stage 1 YSO HH 46 (based on van Kempen et al. 2010b). *Right*: More luminous embedded-source SMM1 (Goicoechea et al. 2011, in preparation). For the latter source, a complete PACS spectral scan has been obtained. For both sources, the fluxes from the central spaxel have been used. The dashed lines give the thermal distribution at the indicated temperatures. The hatched areas in the HH 46 diagram indicate the different physical processes thought to be responsible for the CO emission. See the electronic edition of the *PASP* for a color version of this figure.

plateau in the warm postshock gas in which significant H_2O is produced (Hollenbach & McKee 1989).

The OH chemistry has been further investigated by Wampfler et al. (2010). The $163\ \mu\text{m}$ line seen by PACS toward HH 46 was observed but not detected with HIFI. The upper limit implies a line width of at least $11\ \text{km s}^{-1}$. Inspection of the PACS data for six sources reveals a correlation between the OH and [O I] fluxes, which, together with the broad profiles, is consistent with production in (dissociative) shocks. The relative strengths of the various OH far-infrared lines are remarkably constant from source to source, indicating similar excitation conditions. Only the $119\ \mu\text{m}$ lines connecting with the ground state vary because they are affected by (foreground) absorption. Due to the lack of detected quiescent OH (and H_2O) emission in the HIFI spectra, no abundances in the envelope can yet be determined to test the model predictions of enhanced OH/ H_2O ratios due to X-rays.

The $\text{HDO}/\text{H}_2\text{O}$ ratio has been determined for the low-mass protostar NGC 1333 IRAS2A by Liu et al. (2010). Five HDO lines arising from levels ranging from 20 K up to 170 K have been observed using ground-based telescopes. The inner (>100 K) and outer (<100 K) HDO abundances with respect to H_2 are well constrained to $(0.7\text{--}1.0) \times 10^{-7}$ (3σ) and $(0.1\text{--}1.8) \times 10^{-9}$ (3σ), respectively. If the H_2O and isotopolog lines discussed previously can be associated with the same component as seen in HDO, the inferred limit on the warm H_2O abundance implies a $\text{HDO}/\text{H}_2\text{O}$ abundance higher than $\sim 1\%$ in the inner envelope, consistent with the value found in the hot corino of IRAS16293 ($\sim 3\%$; Parise et al. 2005b). Although absolute abundances of HDO and H_2O jump by more than one order of magnitude between the cold and warm envelopes, the $\text{HDO}/\text{H}_2\text{O}$ ratio in the outer cold envelope is found to have a similar value to that of the inner part, $\sim 1\text{--}18\%$.

The detection of HDO lines in other low-mass protostellar sources has proven difficult from the ground, even under the best weather conditions. Deep *Herschel* observations of high-frequency HDO lines coupled with deep H_2^{18}O data are likely needed to pin down the cold $\text{HDO}/\text{H}_2\text{O}$ ratios. Alternatively, interferometric observations of the higher-excitation HDO lines, coupled with similar data of the H_2^{18}O $3_{13} - 2_{20}$ 203 GHz line (the only H_2^{18}O line readily imaged from the ground; Jørgensen & van Dishoeck 2010a), can constrain the $\text{HDO}/\text{H}_2\text{O}$ ratio in the warm gas in the innermost regions. Initial results by Jørgensen & van Dishoeck (2010b) for the NGC 1333 IRAS4B system indicate much lower values of $< 6 \times 10^{-4}$ than those cited previously for IRAS2A. This large difference is not yet understood.

Overall, it appears that the answer to the first question in § 4.2.1 is that shocks dominate the observed water emission in low-mass YSOs rather than the hot core. Both ice evaporation and high-temperature chemistry are likely important in producing high water abundances in shocks. The answers to the other two questions await more data and analysis.

4.3. Outflows from Low-Mass Young Stellar Objects

4.3.1. Motivation

Deeply embedded protostars drive powerful molecular outflows. These outflows extend over arcminute scales for nearby low-mass objects and can be resolved spatially with *Herschel*. The brightest outflow knots are clearly separated, often by arcminutes, from the dense protostellar envelopes targeted in the low-mass subprogram (§ 4.2). Outflows exhibit a great diversity in their velocity, degree of collimation, opening angle, extent, and gas kinetic temperature (Bachiller & Tafalla 1999), raising the question of whether these characteristics can be linked to the

evolutionary state of the driving sources or whether other parameters (e.g., structure of the protostellar envelope or environment) play a role. In contrast with ground-based observations of low- J CO transitions, *Herschel* data probe the high-excitation regions of the flow, where the hidden jet interacts with surrounding material, and they directly target one of the main coolants, H_2O , thus addressing the shock physics and energetics as a function of distance from the central driving source (Nisini et al. 2000).

Outflows represent a major perturbation in the chemistry of the core gas. In the youngest systems, the SiO , CH_3OH , and H_2O abundances are increased by orders of magnitude as a result of grain destruction and high-temperature gas-phase chemistry. By determining the H_2O abundances in several spatially and kinematically resolved components within a given outflow with HIFI, and by doing this for a sequence of outflows of different ages, the H_2O cycle—from grain mantle, to gas, to mantle—can be reconstructed. This allows a specific puzzle posed by *ISO-LWS* to be addressed; in most protostellar outflow regions, the H_2O abundance is an order of magnitude lower than the value of 10^{-4} expected if high-temperature reactions drive all available gas-phase oxygen into H_2O or if ice mantles evaporate. Ionizing and photodissociative effects of radiation emitted by nearby dissociative shocks may play a critical role in explaining the lower-than-expected shocked H_2O abundances (see also the discussion in Keene et al. 1997; Snell et al. 2005).

Key questions to be addressed in this subprogram are: (1) What is the nature of the flow: dense molecular jets or shocked ambient gas along the cavity walls? Do the characteristics change with distance to the central driving source and with evolution of the system? What is the contribution of water emission to the energy lost in outflows? (2) What is the physical impact of the outflows on their surroundings? The transfer of energy and momentum from the flow to the envelope and cloud plays a critical role in controlling future star formation. (3) What is the chemical effect of the outflows? Can shock-generated UV radiation modify the physics and chemistry of nearby molecular gas? Why is not all oxygen driven into H_2O ?

4.3.2. Source and Line Selection

The outflow subprogram consists of three parts: a survey part, a line excitation part, and spatial maps. In the survey part, 26 flows from stage 0 and stage 1 low-mass YSOs are observed in two H_2O lines—the ground-state $o\text{-H}_2\text{O}$ 557 GHz line with HIFI down to ~ 20 mK and the $179\text{ }\mu\text{m}$ $p\text{-H}_2\text{O}$ line with PACS to similar limits—in two hot spots (blue- and redshifted outflow lobes), providing a statistical basis for the assessment of time evolution effects. The driving sources themselves are covered in the low- and intermediate-mass YSO subprograms (see §§ 4.2 and 4.4). The line excitation survey targets a subsample of three stage 0 outflows for which H_2O emission has previously been detected (L1157, L1448, and VLA1623). These sources are observed in 15 spectral lines with HIFI and PACS

(H_2O , OH, $[\text{O I}]$, and CO) to characterize their physical structure and energy budget. Integration times are such that typically 20–40 mK rms is reached. In the third part, these same three flows are spatially mapped with HIFI down to ~ 20 mK using the on-the-fly mode in the H_2O 557 GHz line to determine the spatial distribution of shocked H_2O and compare it with other outflow tracers like CO, SiO, and CH_3OH . In addition, they are imaged with PACS in the $179\text{ }\mu\text{m}$ line. For NGC 2071, which is known from *Spitzer* data to be particularly rich in H_2O emission (Melnick et al. 2008), full PACS spectral scans are performed at a few positions.

4.3.3. Initial Results

Figure 9 shows the *Herschel*-PACS image of H_2O in the $179\text{ }\mu\text{m}$ line toward the stage 0 source L1157 obtained during the science demonstration phase of *Herschel* (Nisini et al. 2010). PACS spectra at selected positions are included, illustrating the high S/N of the data. The map beautifully reveals where the shocks deposit energy into the molecular cloud, lighting up the water emission along the outflow. The H_2O emission is spatially correlated with that of pure rotational lines of H_2 observed with *Spitzer* (Neufeld et al. 2009) and corresponds well with the peaks of other shock-produced molecules such as SiO and NH_3 along the outflow. In contrast with these species, H_2O is also strong at the source position itself. The analysis of the H_2O $179\text{ }\mu\text{m}$ emission, combined with existing *Odin* and *SWAS* data, shows that water originates in warm compact shocked clumps of

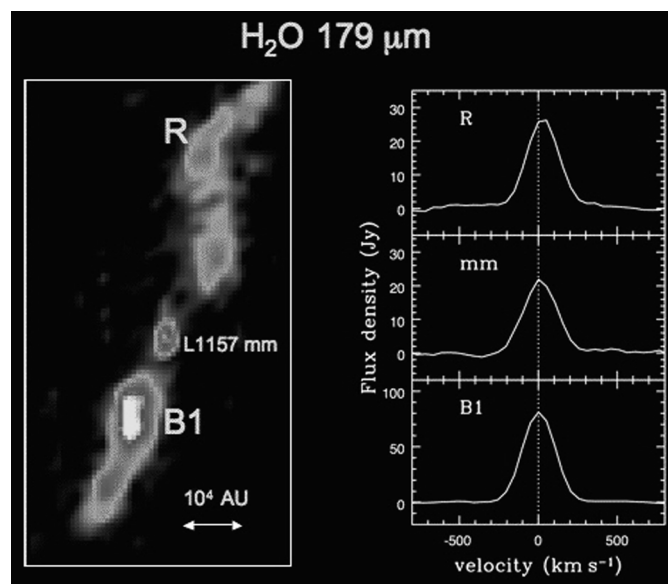


FIG. 9.—*Herschel*-PACS image of the H_2O $179\text{ }\mu\text{m}$ line toward the stage 0 protostar L 1157, together with (spectrally unresolved) PACS spectra at three positions. The water emission is most significant in hot spots along the outflow where the (rotating) jet interacts directly with the cloud, as well as toward the protostar itself (based on Nisini et al. 2010). See the electronic edition of the *PASP* for a color version of this figure.

a few arcseconds in size, where the water abundance is of the order of 10^{-4} : i.e., close to that expected from high-temperature chemistry. The total H_2O cooling amounts to 23% of the total far-IR energy released in shocks estimated from the *ISO*-LWS data (Giannini et al. 2001).

The PACS spectra contained in Figure 9 are spectrally unresolved. HIFI spectra of H_2O and CO at the B1 position in the blue outflow lobe (see Fig. 9) have been presented and analyzed by Lefloch et al. (2010) as part of CHESS, showing that the H_2O abundance increases with shock velocity (see also § 4.2 and Franklin et al. 2008). Codella et al. (2010) propose that this reflects the two mechanisms for producing H_2O : ice evaporation and high-temperature chemistry where the $\text{O} + \text{H}_2$ and $\text{OH} + \text{H}_2$ reactions become significant (see § 2.1 and Fig. 3), with the latter reactions becoming more important at higher velocities. The presence of NH_3 (another grain surface product) seen by Codella et al. (2010) only at lower velocities is consistent with this picture. The WISH data can test this proposed scenario at many more outflow positions.

In summary, the limited data to date illustrate the potential of water to probe and image shock physics and chemistry along the outflows.

4.4. Intermediate-Mass Young Stellar Objects

4.4.1. Motivation

Intermediate-mass YSOs with $\sim 10^2$ – $10^4 L_\odot$ (stellar masses of a few to $10 M_\odot$) form the bridge between the low- and high-mass samples. In addition to covering a significant luminosity range between the two well-studied extremes, intermediate-mass YSOs are interesting in their own right. For example, they are often found in clustered environments, so they can be used as laboratories for investigating high-mass cluster regions which are often more confused, due to their larger distances. Intermediate-mass YSOs may be in an interesting regime when heating from the outside by radiation from neighboring stars is significant compared with internal heating (Jørgensen et al. 2006). This would result in a more extended warm zone and a different chemical structure of the envelope than that of their low- and high-mass counterparts. Also, emerging intermediate-mass YSOs have associated PDRs or reflection nebulae indicating that not only shocks, but also UV photons, play a role in clearing the surroundings. Finally, they are the precursors of Herbig Ae/Be stars, whose protoplanetary disks have been very well studied (e.g., Meeus et al. 2001), but for which very little is known about their formation history.

Key questions are therefore: (1) What is the structure of the envelopes of intermediate-mass YSOs? Do they have a different temperature and chemistry structure compared with their low- and high-mass counterparts? Does the enhanced UV compared with the low-mass counterparts play a role? (2) How do intermediate-mass YSOs evolve? To what extent are the an-

swers to the questions in §§ 4.2, 4.3, 4.5 different for these sources?

4.4.2. Source and Line Selection

Although intermediate-mass YSOs are more energetic than their low-mass counterparts, they are not bright enough to observe at the distances of their high-mass cousins. Surprisingly few nearby (<400 pc) candidates are known, so our team has conducted an active search over the past years to identify a representative sample to observe with HIFI. Six intermediate-mass YSOs with distances of <1 kpc have been selected from this sample, and a significant amount of complementary submillimeter line and continuum observations have been obtained (e.g., Fuente et al. 2005b; Crimier et al. 2010). All of these sources are still at the deeply embedded stage, comparable with stage 0 in the low-mass case. The *Herschel* line selection follows the general criteria outlined previously, and the noise levels are similar to those for the low-mass YSOs.

4.4.3. Initial Results

Observations of various water lines toward NGC 7129 FIRS2 ($430 L_\odot$, 1260 pc) are presented in Fich et al. (2010) and Johnstone et al. (2010), and the two lowest p - H_2O lines detected with HIFI are included in Figure 6. The line profiles are remarkably similar to those of the low-mass YSO NGC 1333 IRAS2A, showing both a broad component (FWHM $\sim 25 \text{ km s}^{-1}$) due to shocks along the outflow cavity and a medium-broad component (FWHM $\sim 6 \text{ km s}^{-1}$) associated with small-scale shocks in the inner dense envelope. Quantitative analysis of all the H_2O and isotopolog lines observed for this object result in an outer-envelope (<100 K) abundance of water of the order of $\sim 10^{-7}$, an order of magnitude higher than for the low- and high-mass YSOs. Alternatively, both the high- J CO and H_2O lines seen with HIFI and PACS can be analyzed in a single slab model with a temperature of ~ 1000 K and density of $\sim 10^7$ – 10^8 cm^{-3} , representative of a shock in the inner dense envelope (Fich et al. 2010). This leads to a typical $\text{H}_2\text{O}/\text{CO}$ abundance ratio of 0.2–0.5.

The results for this first source demonstrate that the observing strategy for this subprogram is sound and that the data can provide the quantitative information to answer the preceding questions, once more sources have been observed and analyzed.

4.5. High-Mass Young Stellar Objects

4.5.1. Motivation

High-mass stars ($>10 M_\odot$ and $>10^4 L_\odot$), though few in number, play a major role in the energy budget and shaping of the Galactic environment (e.g., Cesaroni et al. 2005). These are also the type of regions that dominate far-infrared observations of starburst galaxies. Their formation is not at all well

understood, due to large distances, short timescales, and heavy extinction.

Recent results show that the embedded phase of the formation of O and B stars can be divided empirically into several classes. The earliest stage are the massive prestellar cores, which are local temperature minima and density maxima and which represent the initial conditions. Their observational characteristics are large column densities, low temperatures, and absence of outflow or maser activity. The next stage are the high-mass protostellar objects (HMPOs), where the central star is surrounded by a massive envelope with a centrally peaked temperature and density distribution. HMPOs show signs of active star formation through outflows and/or masers. This sub-program distinguishes mid-IR-bright and mid-IR-quiet objects with a boundary of 10 Jy at 12 μ m. The next evolutionary phase is represented by hot molecular cores, with large masses of warm and dense dust and gas and with high abundances of complex organic molecules evaporated off dust grains. Hot molecular cores have regions of $T > 100$ K that are >0.1 pc in size. The final stages considered here are ultracompact H II regions (UC H II), where large pockets of ionized gas have developed but are still confined to the star. UC H II sources have free-free flux densities of more than a few millijanskys (for a distance of a few kiloparsecs) and sizes of 0.01–0.1 pc. As with the previous category, this criterion may imply a luminosity of $>10^5 L_{\odot}$. The embedded phase ends when the ionized gas expands hydrodynamically and disrupts the parental molecular cloud, producing a classical H II region. Although the evolutionary path of high-mass YSOs likely runs through these different categories, this is not yet as well established as for the case of low-mass YSOs, and the physical structure and processes dominating each of these stages are not well characterized. *Herschel* observations of water and related species will provide an important piece of this puzzle.

Abundant H₂O has been observed with *ISO*, *SWAS*, and *Odin* toward the Orion and SgrB2 high-mass star-forming regions (e.g., Cernicharo et al. 2006; Polehampton et al. 2007; Persson et al. 2007). Toward other high-mass YSOs, copious hot gas phase H₂O has been detected in absorption with *ISO-SWS* (van Dishoeck & Helmich 1996; Boonman & van Dishoeck 2003) but not with *ISO-LWS*. *SWAS* data indicate generally weak H₂O 557 GHz emission (Snell et al. 2000). Analysis of these data for selected high-mass star-forming regions implies sharp gradients in the water abundance, together with strong excitation changes, but their origin is not yet well understood (Boonman et al. 2003; van der Tak et al. 2006). More generally, the role of shocks and the relative importance of shocks versus passive heating in the inner envelope during the high-mass evolution, either in isolated sources or in clusters, is currently unclear. In addition, the relation of these phases to the H₂O maser sources needs further study. Since individual high-mass sources are at much larger distances (typically a few kiloparsecs) than their low-mass counterparts and thus

spatially unresolved, disentangling the various processes requires observations of numerous H₂O transitions and high spectral resolution, as obtained within WISH using HIFI and PACS.

Key questions include: (1) What is the chemistry of the warm gas close to young high-mass stars in various evolutionary stages, specifically the distribution of H₂O? (2) What is the relative importance of shocks vs. UV for the interaction of the stars with their environment? (3) What are the kinematics of the cold and warm gas close to young high-mass stars? (4) What are the effects of clustered star formation and feedback by protostellar outflows on high-mass regions?

4.5.2. Source and Line Selection

The WISH observations of H₂O and related species cover each of the preceding phases in the formation of high-mass stars. Pointed observations with HIFI are made of a sample of four massive prestellar cores and 19 protostellar sources. The prestellar cores are taken from Carey et al. (1998) and Pillai et al. (2006a) and are observed only in the 557 GHz line down to 10 mK rms. The protostellar list consists of 10 HMPOs (five midinfrared bright and five quiet), four hot cores, and five UC H II regions. The sources are nearby (less than a few kiloparsecs) and isolated, selected from surveys by Molinari et al. (1996), Sridharan et al. (2002), Wood & Churchwell (1989), and van der Tak et al. (2000b). The basic H₂O line list is the same as for the low-mass and intermediate-mass YSOs, but with additional H₂¹⁸O and H₂¹⁷O lines added, because the main isotopic lines are very bright and highly optically thick. Absorption lines of H₂O at high frequencies against the optically thick continuum can uniquely probe the kinematics of the protostellar environment (see § 2.2). Integration times are such that 50–150 mK rms is reached, depending on the line.

Full PACS spectral scans of all protostellar sources are taken and provide an unbiased overview of low- and high-excitation H₂O lines (and thus the shocked ~ 1000 K gas in the beam), together with OH, [O I], and CO at the position of the protostar, as well as spatial information on a 50'' scale. S/N >100 on the continuum are reached so that spectrally unresolved lines can be detected. To characterize the effects of clustered star formation and feedback, including the chemistry and cooling rates of intracluster gas, HIFI mapping of the *p*-H₂O 1113 GHz line combined with ¹³CO 10–9 plus PACS mapping of *o*-H₂O 1670 and 1717 GHz down to 300 mK rms is planned over a region of $\sim 3' \times 3'$ for six nearby cluster-forming clouds, where several hot cores and UC H II regions are known to coexist in a small area.

4.5.3. Initial Results

Figure 6 includes the lowest two *p*-H₂O lines for the high-mass YSO W3 IRS5 (Chavarría et al. 2010). The profile of the excited $2_{02} - 1_{11}$ line reveals the same broad and medium-broad

components as seen for their low- and intermediate-mass counterparts, but the profile of the ground-state line is clearly more complex. In addition to self-absorption and absorption of the cold envelope against the continuum, absorptions due to foreground clouds lying along the line of sight are seen at various velocities. Moreover, for line-rich sources, weak emission lines due to species other than H_2O are detected. The ability of HIFI to disentangle the different physical components is demonstrated by initial performance verification data on DR21 (OH) (van der Tak et al. 2010). Using a slab model and assuming an o/p ratio of 3 (Lis et al. 2010), the broad component due to the outflow is found to have an H_2O abundance of a few $\times 10^{-6}$. Water is much less abundant in the foreground cloud, where $p\text{-H}_2\text{O}$ has an abundance of 4×10^{-9} . The outer-envelope abundance is even lower: a few $\times 10^{-10}$.

To investigate whether these abundances are typical of high-mass protostellar sources, Marseille et al. (2010) model four additional high-mass YSOs in the lowest two $p\text{-H}_2^{18}\text{O}$ lines combined with the ground-state $p\text{-H}_2^{18}\text{O}$ line. Due to the high spectral resolution, the envelope emission and absorption can be cleanly separated from other physical components. Chavarría et al. (2010) analyze a larger set of lines for W3 IRS5. Since the same modeling philosophy is used for all six sources, the inferred abundances can be directly compared. The outer-envelope water abundances are low in all cases but show a 2-order-of-magnitude variation from $<5 \times 10^{-10}$ to 4×10^{-8} . The origin for these variations is not yet understood, since no correlation is found with luminosity or evolutionary stage within this small sample. For W3 IRS5, a jump in abundance in the inner envelope at $T \approx 100$ K is inferred from the isotopolog lines, which is the only indication so far of water emission from a hot core.

Broad emission profiles due to outflows associated with the high-mass protostars are commonly seen in the high-mass spectra, testifying to the importance of shocks. Moreover, the presence of blueshifted absorption suggests expansion of the outer envelope, rather than infall. Finally, the high S/N absorption data reveal cold clouds surrounding the protostellar envelope at velocities offset by just a few kilometers per second, illustrating the complexity of the protostellar environment and the unique ability of HIFI and water to detect this gas (Marseille et al. 2010).

In summary, the available data on the first six sources show that questions 1 and 3 in § 4.5.1 can be addressed quantitatively. Questions 2 and 4 require more data to answer.

4.6. Radiation Diagnostics

4.6.1. Motivation

The H_2O chemistry can be strongly affected by high-energy radiation from YSOs, both UV and X-rays. For typical X-ray luminosities of $10^{28}\text{--}10^{31}$ ergs s^{-1} appropriate for low-mass YSOs, models show that the H_2O abundance decreases by 2 orders of magnitude or more in the inner envelope, where

the X-rays penetrate up to distances of ~ 1000 AU (one *Herschel* beam; Stäuber et al. 2006). UV and X-rays also affect the chemistry in high-mass YSO envelopes, but to a different degree (Stäuber et al. 2004, 2005). H_2O is destroyed not only by direct photodissociation but also by reactions with ionized molecules, so that it is important to understand their chemistry in relation to that of H_2O (Fig. 3). Because H_2O is not a unique diagnostic of either UV or X-rays, independent diagnostics need to be observed. Small hydrides, especially OH^+ , CH , CH^+ , and SH^+ , are particularly powerful in this regard (Stäuber et al. 2005; Bruderer et al. 2010a). Recent 2D modeling has shown that most of the emission from UV tracers originates in the outflow walls, where their abundances are enhanced by orders of magnitude due to UV impinging on the walls of the outflow cavities leading to ionization, dissociation, and high-temperature chemistry (Bruderer et al. 2009b, 2009a, 2010a).

Key questions are: (1) Can we establish the presence of UV and/or X-rays through chemistry in deeply embedded objects, where the UV or X-rays cannot be observed directly? If so, can we quantify it? (2) How do protostellar UV and X-rays influence the surroundings, both the temperature and the water chemistry?

4.6.2. Source and Line Selection

Deep pointed observations with HIFI are made of lines of seven hydrides that are related to the water network and are sensitive to either FUV or X-rays (or both) in two high-mass and one low-mass YSO down to 15 mK rms. Subsequently, a larger sample of nine low-, intermediate-, and high-mass YSOs is surveyed in the lines of CH , CH^+ , and OH^+ . Lines of some hydrides are also obtained serendipitously with the main H_2O settings in the other subprograms. For example, the CH 536 GHz triplet is often obtained together with the $o\text{-H}_2^{18}\text{O}$ $1_{10} - 1_{01}$ 548 GHz line and the H_2O^+ $1_{11} - 0_{00}$ 1115 GHz line with the $p\text{-H}_2\text{O}$ $1_{11} - 0_{00}$ 1113 GHz line. Line frequencies have been collected, and in some cases first predicted, by Bruderer (2006).

4.6.3. Initial Results

An early surprise from all *Herschel*-HIFI KPs is the detection of widespread H_2O^+ absorption in a variety of Galactic sources including diffuse clouds, the envelopes of massive YSOs and outflows (Gerin et al. 2010; Ossenkopf et al. 2010; Benz et al. 2010; Bruderer et al. 2010b; Wyrowski et al. 2010b; Neufeld et al. 2010; Schilke et al. 2010; Gupta et al. 2010). H_2O^+ and OH^+ lines are even seen in emission in Spectral and Photometric Imaging Receiver Fourier Transform Spectrometer spectra of the active galactic nucleus Mkr231 (van der Werf et al. 2010). Model analyses point to an origin in low-density gas ($<10^4$ cm^{-3}) with a low molecular fraction (i.e., a H_2/H ratio of a few percent) to prevent H_2O^+ from reacting rapidly with H_2 to form H_3O^+ . The low molecular fraction can be the result of either high UV or high X-ray fluxes.

Within WISH, deep integrations on two high-mass YSOs reveal most of the targeted molecules, which is a vindication of the model predictions. CH, NH, OH⁺, and H₂O⁺ are detected toward both W3 IRS5 and AFGL 2591 (Benz et al. 2010; Bruderer et al. 2010b). In addition, SH⁺ and H₃O⁺ are seen toward W3 and CH⁺ is seen toward AFGL 2591. Only SH and NH⁺ are not detected. H₂O⁺, OH⁺, and SH⁺ are new molecules, with OH⁺ and SH⁺ only recently detected for the first time in ground-based observations by Wyrowski et al. (2010a) and Menten et al. (2011), respectively. Figure 10 contains a collection of spectra of hydrides most closely related to water.

The spectra show a surprising mix of absorption and emission features. Three molecules, NH, OH⁺, and H₂O⁺, appear

primarily in absorption, either in diffuse foreground clouds along the line of sight, in blueshifted outflows, or (in some cases) in clouds close to the systemic velocity. For these molecules, the $J = 1$ level lies at 47 K or higher. Limits on the excited state lines give rotational temperatures <13 and <19 K for OH⁺ and H₂O⁺, respectively. CH and SH⁺, for which the $J = 1$ line lies at less than 26 K, are seen in emission, although CH has superposed absorption. The CH⁺ $J = 1-0$ line occurs mostly in absorption, but the 2–1 line is in emission in AFGL 2591. For W3 IRS5, at least three H₃O⁺ lines from energy levels lying at a few hundred degrees Kelvin above ground are detected, which combined with ground-based data (Phillips et al. 1992) give a rotational temperature of 240 ± 40 K. Note

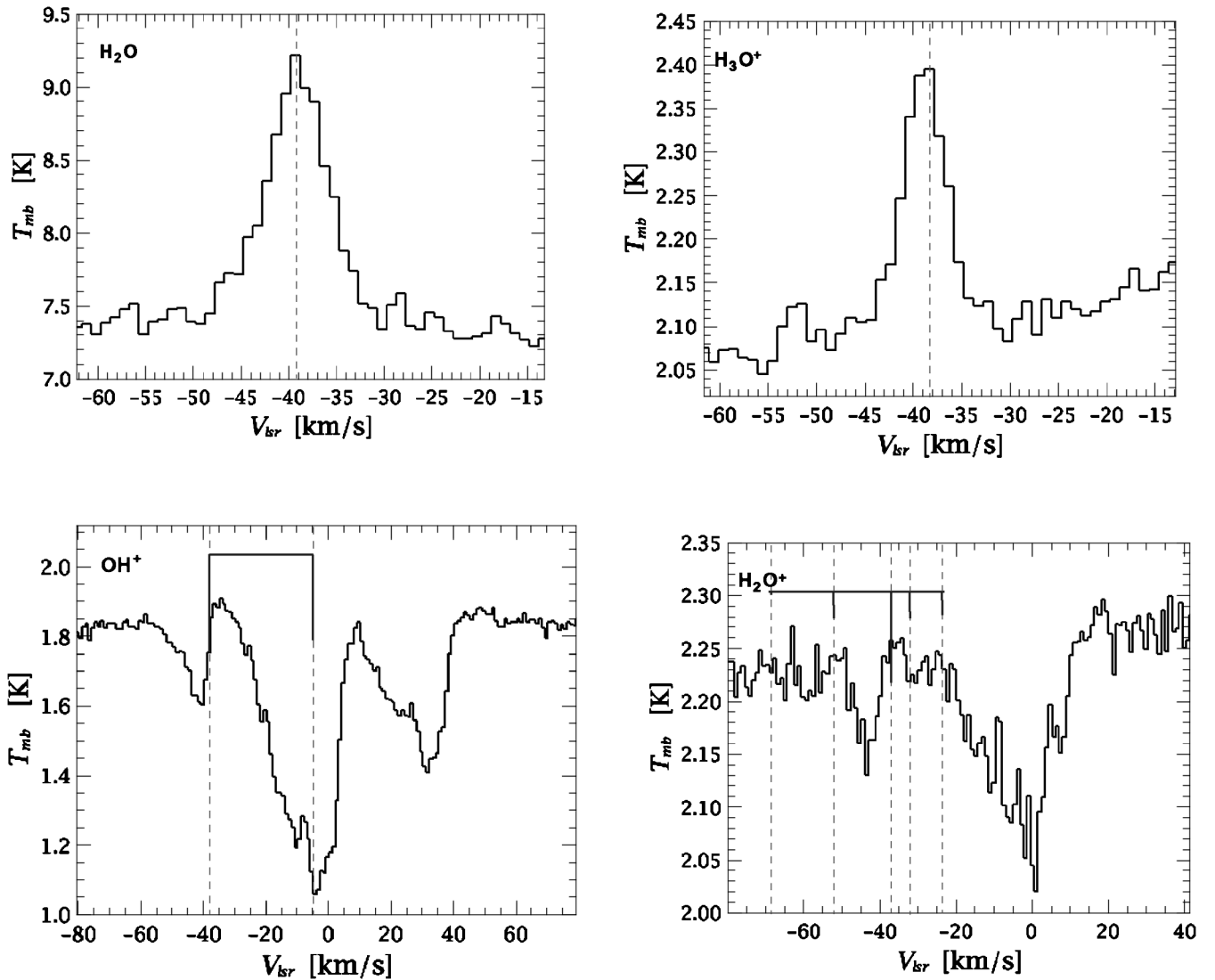


FIG. 10.—Collection of lines of hydrides related to the H₂O chemistry detected toward the high-mass YSO W3 IRS5 (based on Benz et al. 2010). The dashed lines indicate the position of the main component at the LSR velocity of the protostellar envelope at -38.4 km s⁻¹. For species with fine-structure components (OH⁺ and H₂O⁺), the lengths of the vertical bars indicate the theoretical relative intensities. Note that strong OH⁺ and H₂O⁺ absorption occurs around $V_{\text{LSR}} \approx 0$ km s⁻¹ in diffuse foreground clouds. The H₂O line is $3_{31} - 4_{04}$ at 1894 GHz; H₃O⁺ is $4_{20} - 3_{21}$ at 1069 GHz. See the electronic edition of the *PASP* for a color version of this figure.

that all excitation temperatures are lower limits to the kinetic temperature of the gas, because the lines have high critical densities ($>10^7 \text{ cm}^{-3}$), resulting in subthermal excitation.

The observed range in line profiles and excitation conditions immediately indicates that the species originate in different parts of the YSO environment. The $\text{OH}^+/\text{H}_2\text{O}^+$ abundance ratio of >1 for the blueshifted gas in both sources indicates low-density and high-UV fields (Gerin et al. 2010), as expected along the cavity walls at large distances from the source. The CH , CH^+ , and H_3O^+ emission lines must originate closer to the protostar, at densities $>10^6 \text{ cm}^{-3}$ (Bruderer et al. 2010b). Their abundances are roughly consistent with the 2D photochemical models, in which high-temperature chemistry and high UV fluxes boost their abundances along the outflow walls (Bruderer et al. 2009a, 2010a). The UV field is enhanced by at least 4 orders of magnitude compared with the general interstellar radiation field in these regions.

Because the H_2O^+ ground-state line occurs close to that of $p\text{-H}_2\text{O}$, observations of both species are available for a large sample of high-mass protostars within WISH. Using also H_2^{18}O data, Wyrowski et al. (2010b) provide column densities for both species for all components along 10 lines of sight. H_2O^+ is always in absorption, even when H_2O is seen in emission. Consistent with the preceding scenario, the highest H_2O^+ column densities are found for the outflow components. Overall, $\text{H}_2\text{O}^+/\text{H}_2\text{O}$ ratios range from 0.01 to >1 , with the lower values found in the dense protostellar envelopes and the larger values found in diffuse foreground clouds and outflows.

In summary, most of the targeted hydrides are readily detected and they appear to be even more abundant and widespread than expected prior to *Herschel*. When associated with protostars, they trace regions of high temperatures and enhanced UV fluxes, such as those found along cavity outflow walls. However, the fact that some hydrides are seen in absorption whereas others appear in emission is not yet fully understood.

4.7. Circumstellar Disks

4.7.1. Motivation

A fraction of the gas and dust from the protostellar envelope ends up in a rotating disk around the pre-main-sequence star ($\leq 10 \text{ Myr}$), thereby providing the basic material from which planetary systems can be formed. Recent observations and modeling have shown that many young disks have a strongly flaring structure in which the surface layers are exposed to intense ultraviolet radiation from the star. This results in a highly layered structure with a hot top layer that is mostly atomic, due to rapid photodissociation; an intermediate warm layer with an active chemistry and that is responsible for most of the observed molecular emission; and a cold, dense midplane layer where most species are frozen out onto grains (e.g., Aikawa et al. 2002; Bergin et al. 2007).

A major question in disk-evolution and planet-formation studies is the amount of grain growth and vertical mixing as a function of radial position and time. In the static models described previously, little gas-phase H_2O is expected in the outer disk, with most of it frozen out as H_2O ice in the midplane. However, if the H_2O ice is regularly circulated to the warmer upper layers, the gas-phase H_2O abundance increases by orders of magnitude (Dominik et al. 2005). This in turn affects the gas temperature and the abundances of other species, including its photodissociation products OH and O . Indeed, analysis of CO observations shows that significant gaseous CO is present at temperatures below that for freeze-out (e.g., Dartois et al. 2003). Both photodesorption of ices and rapid vertical mixing combined with a steep vertical temperature gradient and grain growth have been invoked to explain this (Aikawa 2007; Öberg et al. 2007; Hersant et al. 2009).

HIFI observations are uniquely suited to constrain vertical mixing models, because H_2O is the major ice reservoir and its line emission is particularly sensitive to temperature. HIFI thus probes the cold H_2O gas reservoir in the outer ($>30 \text{ AU}$) part of disks. These observations are therefore highly complementary to *Spitzer* detections of hot H_2O lines that originate in the inner few AU of disks (Salyk et al. 2008; Carr & Najita 2008). Key questions are: (1) What do H_2O observations of circumstellar disks tell us about grain growth and the importance of vertical mixing from the cold midplane to the warm surface layers where ices photodesorb or thermally vaporate? (2) What is the relative importance of photodissociation and desorption? (3) What are the implications of the *Herschel* observations of the cold water reservoir in disks for the transport of water to the inner planet-forming zones of disks?

4.7.2. Source and Line Selection

Deep integrations down to a $\sim 1.5 \text{ mK rms}$ in 0.5 km s^{-1} bin are performed for the $o\text{-H}_2\text{O}$ 557 GHz line in four targets (TW Hya, DM Tau, LkCa15, and MWC 480) and down to $\sim 4 \text{ mK rms}$ for the $p\text{-H}_2\text{O}$ 1113 GHz line in two targets (TW Hya and DM Tau). The primary aim of these very deep integrations is to put stringent limits on the *cold* water reservoir. Shorter integrations down to 10 mK rms in the 557 GHz line are performed for eight additional targets to determine whether the four deep targets are unusual in their H_2O emission. The excited $\text{H}_2\text{O } 3_{12} - 3_{03}$ 1097 GHz and CO $J = 10 - 9$ lines are observed in two sources to probe the warmer H_2O reservoir with HIFI. Sources have been selected to be clean from surrounding cloud emission in single-dish observations (e.g., Thi et al. 2001).

4.7.3. Initial Results

Deep integrations on the DM Tau disk show a tentative detection of the $o\text{-H}_2\text{O}$ line with a peak temperature of $T_{\text{MB}} = 2.7 \text{ mK}$ and a width of 5.6 km s^{-1} (Bergin et al. 2010b).

Regardless of the reality of this detection and the uncertainty in the collisional rate coefficients, the inferred column density is a factor of 20–130 weaker than that predicted by a simple model in which gaseous water is produced by photodesorption of icy grains in the UV illuminated regions of the disk (Dominik et al. 2005). The most plausible implication of this lack of water vapor is that more than 95–99% of the water ice is locked up in large coagulated grains that have settled to the midplane and are not cycled back up to the higher disk layers. Thus, the deep HIFI data can directly address the key questions of this subprogram, even without actual detections.

5. DISCUSSION

Although less than 10% of the WISH data have been analyzed to date, several general trends are emerging.

5.1. Trends with Evolutionary Stage

The development of the spectral features with evolutionary phase is illustrated by Figure 4 for low-mass sources. Water emission is not detected from cold dense cores prior to star formation, down to very low levels. The implication is that most of the water is frozen out as ice on dust grains in the densest regions with, at most, a small layer of water vapor due to photodesorption of ice in the outer regions of the core. As soon as the protostar turns on in the center, however, prominent H_2O lines appear. One of the main surprises for the low-mass YSOs is that this emission has broad profiles, even for H_2^{18}O , indicating an origin in shocked gas. This association with outflows is directly revealed by imaging of the water line (Fig. 9). H_2O abundances in the outflow are high, of the order of $10^{-5} - 10^{-4}$ (assuming a CO/H_2 abundance ratio of 10^{-4}), increasing with higher velocity. In contrast, quiescent envelope abundances, as derived from narrow absorption features and the lack of narrow H_2^{18}O emission, are low, of the order of 10^{-8} .

The last evolutionary stage of protoplanetary disks when the envelope has dissipated again shows little H_2O emission down to very low levels (Fig. 4). This is the first time that the cold water reservoir in the outer regions of disks has been probed. The lack of emission implies that the upper layers of this disk are surprisingly dry, both in the gas and in the solid phases. About 95–99% of the water ice appears to be contained in large icy grains in the disk midplane, which are not cycled back up to higher layers. If confirmed by observations of additional sources, this may have profound implications for our understanding of the chemistry and physics of the outer disks. On the other hand, lines of warm and hot water have been detected in other disks with *Spitzer* (Pontoppidan et al. 2010) and with PACS (Sturm et al. 2010), although the latter detection needs confirmation. Tying these data together should provide a nearly complete view of the distribution of water vapor from the inner to the outer disk.

For all of these stages, the availability of data on both *o*- H_2O and *p*- H_2O indicates that the low water abundance is robust and independent of any *o/p* ratio of water. The overall emerging picture is therefore that most water is formed on grains in the molecular cloud and prestellar core phases, is present mostly as ice in the quiescent envelope, and is likely transported in this form into the outer part of young disks without further evaporation, consistent with evolutionary models by Visser et al. (2011, in preparation).

5.2. Trends with Luminosity

Figure 6 illustrates the trend with luminosity for the embedded protostellar evolution stage. An initial conclusion is that the line profiles are remarkably similar in spite of the 4-order-of-magnitude range in luminosity. All profiles show a broad (FWHM $25\text{--}40\text{ km s}^{-1}$) component due to the shocks along the outflow cavity walls on scales $>1000\text{ AU}$ (shell shocks) and a medium-broad (FWHM $5\text{--}10\text{ km s}^{-1}$) component ascribed to shocks caused by the interaction of jets and winds with the inner dense ($>10^6\text{ cm}^{-3}$) envelope on scales $<1000\text{ AU}$. Thus, the processes by which the jets and winds that are launched close to the star interact with their environment are apparently similar across a wide range of masses and luminosities. The H_2O medium-broad profiles clearly have larger line widths than those of other high-density envelope tracers such as HCO^+ 4–3 and CS 7–6, but generally agree with the profiles of other grain surface products such as CH_3OH .

For low- and intermediate-mass YSOs, the outflows dominate the H_2O emission, whereas for high-mass YSOs, narrower lines from the passively heated envelope become more prominent, especially for H_2^{18}O and H_2^{17}O . Inferred outer-envelope abundances based on the isotopolog data and narrow absorption features vary between 10^{-8} and 10^{-10} with no obvious trends across luminosity or evolutionary stage, except for a potentially higher value for one intermediate-mass source. These low abundances thus confirm the earlier *SWAS* conclusions, but can significantly refine them because of the availability of more lines from both *o*- and *p*- H_2O , allowing more accurate determinations. Because of the dominance of outflow emission, it is more difficult than expected to put firm constraints on the inner quiescent hot-core water abundances. Generally, the stirred-up inner region probed by the medium-broad component overwhelms any hot-core emission, even though this warm quiescent gas is clearly seen in, for example, $\text{C}^{18}\text{O } J = 9\text{--}8$ or $10\text{--}9$ emission. Simultaneous analysis of these CO high- J data with the H_2O lines may help to further disentangle the components. Indeed, the coverage of the entire CO ladder up to $J = 44$ with all three instruments on *Herschel* will soon become one of the most important diagnostics to characterize the physical processes in a wide variety of sources.

The PACS and HIFI observations of high- J CO, H_2O , and $[\text{O I}]$ illustrate the need for the development of multidimensional models that include UV photon and shock heating along the

cavity walls for both low- and high-mass sources. This need is strengthened by the detection of various hydrides enhanced by UV radiation, including OH^+ , H_2O^+ , SH^+ , CH , and CH^+ . Initial quantitative estimates of the total far-infrared line emission indicate that H_2O is not the major coolant of the gas, even in the densest ($>10^6 \text{ cm}^{-3}$) regions, but this needs to be confirmed by observational data at more positions, both on and off source. $[\text{O I}]$ and OH have higher luminosities and appear to trace a dissociative shock in the densest inner part.

5.3. Water Chemistry

The *Herschel* data demonstrate that all three chemical networks illustrated in Figure 3 are important in star-forming regions. Solid-state chemistry dominates in the coldest regions, as evidenced by the absence of H_2O line emission from cold prestellar cores and the low gaseous water abundances in the outer protostellar envelopes. Most of the water is in the form of ice formed through the reactions illustrated in the bottom part of Figure 3. The tiny amounts of water gas detected with HIFI either result from nonthermal desorption of water ice, or from gas-phase ion-molecule reactions, or from a combination of both. If the absorption of H_2O gas toward the prestellar core L1544 is confirmed, this first direct detection of water vapor in a quiescent dark cloud will allow a quantitative test of these chemical models. Similarly, a thorough analysis of the abundance structure of H_2O gas and ice for those protostellar envelopes where both species are detected can test key aspects of the cold chemistry. Eventually, fully coupled time-dependent gas-grain chemistry models should include the new solid-state laboratory data on water ice formation. Such models can then also be used to interpret the puzzling $\text{HDO}/\text{H}_2\text{O}$ abundance ratios found in different regions.

The detection of *all* the hydrides involved in the ion-molecule scheme leading to water— OH^+ , H_2O^+ , H_3O^+ , HCO^+ , and OH —will be one of the lasting legacies of the *Herschel* mission. While these species have been part of the reaction networks for decades, the ease with which rapidly reacting ions such as OH^+ and H_2O^+ are detected has surprised even the astrochemists. Since all key reaction rates involved are well understood, the abundance ratios can be used to probe the physics of the regions in which they are found, such as high-UV fields and low densities. The final clue to the basic oxygen gas-phase chemistry network will be provided by deep searches for O_2 , which are planned for some of the WISH sources in other key programs.

The bright water emission from protostars is dominated by C-type shocks where the temperature rises to a few thousand degrees Kelvin. The high-quality line profiles may allow the two chemical regimes to be separated: sputtering of icy mantles and high-temperature chemistry. Whether all available oxygen is driven into water at the highest temperatures and velocities is still an open question. $\text{OH}/\text{H}_2\text{O}$ ratios derived from velocity-resolved OH line profiles could form a powerful test of the neutral-neutral reactions. If the contribution from dissociative

J-type shocks can be cleanly separated, as appears to be the case for HH 46, the observed O/OH abundance ratios would provide a further test of the high-temperature gas-phase reaction networks, but now under conditions with much higher H/H_2 ratios in the presence of UV radiation.

Finally, all three chemical networks play a role in the water chemistry in disks, with high-temperature chemistry dominating in the inner disk and ice chemistry dominating in the outer disk. Here, *Herschel* teaches us another lesson: the importance of coupling the water chemistry with the dynamics and physical evolution of the disks—in particular, the growth and settling of the icy grains to the midplane.

6. CONCLUSIONS

The goal of the WISH program is to use water and related species as physical and chemical probes of star-forming regions over a range of luminosities and evolutionary stages. The initial results presented in § 4 and discussed in § 5 demonstrate that many of the questions asked in the individual subprograms can indeed be addressed by the WISH data, due to the combination of excellent sensitivity, fully resolved line profiles, and spatial information, thereby validating the observational strategy. Initial surprises include a near absence of gaseous water in prestellar cores and disks, the dominance of shocks rather than hot cores in controlling the bright water emission from protostars, and the detection of all of the ions and hydrides involved in the water chemistry schemes. For prestellar cores our observations are in agreement with models that suggest near total freeze-out of water in the form of ice, whereas in disks the inferred water abundance is at levels significantly lower than predicted. So far, water has not yet been found to be the major coolant in any of these regions. All remaining observations are expected to be taken within the next year. Quantitative analysis will require the further development of multidimensional models of protostellar envelopes, outflows, and disks. Together with the results from related *Herschel* key programs, they will greatly enhance our understanding of water in the Galactic interstellar medium and solar system and will provide a true legacy to follow the water trail from the most diffuse gas to dense cores and disks—and eventually comets and planets in our own solar system.

The authors are grateful to the HIFI project scientist, Xander Tielens, for helping to ensure the powerful HIFI capabilities for water observations and for his encouragements over the last decade. They salute the HIFI and PACS instrument builders for providing two superb scientific instruments, and they are much indebted to the laboratory and theoretical chemistry groups for providing the necessary molecular data to analyze and interpret the water data. They thank the referee, David Hollenbach, for his constructive comments on the manuscript, Laurent Wiesenfeld for helpful discussions on the $\text{H}_2\text{O} - \text{H}_2$ collisional rate coefficients, and many funding agencies for their financial support. HIFI has been designed and built by a consortium

of institutes and university departments from across Europe, Canada, and the United States under the leadership of SRON Netherlands Institute for Space Research (Groningen, The Netherlands) and with major contributions from Germany, France, and the United States. Consortium members are Canada: CSA and University of Waterloo; France: CESR, LAB, LERMA, and IRAM; Germany: KOSMA, MPIfR, and MPS; Ireland: NUI Maynooth; Italy: ASI, IFSI-INAF, and Osservatorio Astrofisico di Arcetri-INAF; Netherlands: SRON and TUD; Poland: CAMK and CBK; Spain: Observatorio Astronómico Nacional (IGN) and Centro de Astrobiología (CSIC-INTA).

Sweden: Chalmers University of Technology-MC2, RSS & GARD, Onsala Space Observatory, Swedish National Space Board, and Stockholm University—Stockholm Observatory; Switzerland: ETH Zurich and FHNW; United States: California Institute of Technology, Jet Propulsion Laboratory, and NHSC. HCSS/HSpot/HIPE are joint developments by the Herschel Science Ground Segment Consortium, consisting of ESA, the NASA Herschel Science Center, and the Heterodyne Instrument for the Far-Infrared (HIFI), Photoconducting Array Camera and Spectrometer (PACS) and Spectral and Photometric Imaging Receiver (SPIRE) consortia.

REFERENCES

- Aikawa, Y. 2007, *ApJ*, 656, L93
- Aikawa, Y., Herbst, E., Roberts, H., & Caselli, P. 2005, *ApJ*, 620, 330
- Aikawa, Y., van Zadelhoff, G. J., van Dishoeck, E. F., & Herbst, E. 2002, *A&A*, 386, 622
- Aikawa, Y., Wakelam, V., Garrod, R. T., & Herbst, E. 2008, *ApJ*, 674, 984
- André, P., & Montmerle, T. 1994, *ApJ*, 420, 837
- André, P., Ward-Thompson, D., & Barsony, M. 2000, in *Protostars and Planets IV*, ed. V. Mannings, A. P. Boss, & S. S. Russell (Tucson: Univ. of Arizona), 59
- Atkinson, R., Baulch, D., Cox, R., Crowley, J., Hampson, R., & Hynes, R. 2004, *Atmos. Chem. Phys.*, 4, 1461
- Bachiller, R., Codella, C., Colomer, F., Liechti, S., & Walmsley, C. M. 1998, *A&A*, 335, 266
- Bachiller, R., & Tafalla, M. 1999, *The Origin of Stars and Planetary Systems*, ed. C. J. Lada, & N. D. Kylafis (NATO ASI Ser. C, 540; Dordrecht: Kluwer), 227
- Beltrán, M. T., Cesaroni, R., Neri, R., Codella, C., Furuya, R. S., Testi, L., & Olmi, L. 2005, *A&A*, 435, 901
- Benz, A. O., Stäuber, P., Bourke, T. L., van der Tak, F. F. S., van Dishoeck, E. F., & Jørgensen, J. K. 2007, *A&A*, 475, 549
- Benz, A. O., et al. 2010, *A&A*, 521, L35
- Bergin, E. A., Aikawa, Y., Blake, G. A., & van Dishoeck, E. F. 2007, in *Protostars and Planets V*, ed. B. Reipurth, D. Jewitt, & K. Keil (Tucson: Univ. of Arizona), 751
- Bergin, E. A., Alves, J., Huard, T., & Lada, C. J. 2002, *ApJ*, 570, L101
- Bergin, E. A., & Snell, R. L. 2002, *ApJ*, 581, L105
- Bergin, E. A., & Tafalla, M. 2007, *ARA&A*, 45, 339
- Bergin, E. A., et al. 2000, *ApJ*, 539, L129
- . 2010a, *A&A*, 521, L20
- . 2010b, *A&A*, 521, L33
- Beuther, H., Schilke, P., Gueth, F., McCaughrean, M., Andersen, M., Sridharan, T. K., & Menten, K. M. 2002a, *A&A*, 387, 931
- Beuther, H., Schilke, P., Menten, K. M., Motte, F., Sridharan, T. K., & Wyrowski, F. 2002b, *ApJ*, 566, 945
- Beuther, H., Walsh, A. J., Thorwirth, S., Zhang, Q., Hunter, T. R., Megeath, S. T., & Menten, K. M. 2008, *A&A*, 481, 169
- Beuther, H., Zhang, Q., Bergin, E. A., Sridharan, T. K., Hunter, T. R., & Leurini, S. 2007, *A&A*, 468, 1045
- Bjerkeli, P., et al. 2009, *A&A*, 507, 1455
- Bockelée-Morvan, D., et al. 1998, *Icarus*, 133, 147
- Boogert, A. C. A., et al. 2008, *ApJ*, 678, 985
- Boonman, A. M. S., Doty, S. D., van Dishoeck, E. F., Bergin, E. A., Melnick, G. J., Wright, C. M., & Stark, R. 2003a, *A&A*, 406, 937
- Boonman, A. M. S., & van Dishoeck, E. F. 2003b, *A&A*, 403, 1003
- Brinch, C., Crapsi, A., Hogerheijde, M. R., & Jørgensen, J. K. 2007, *A&A*, 461, 1037
- Brinch, C., & Hogerheijde, M. R. 2010, *A&A*, 523, A25
- Bronfman, L., Nyman, L., & May, J. 1996, *A&AS*, 115, 81
- Bruderer, S. 2006, M.S. thesis, ETH Zurich (Switzerland)
- Bruderer, S., Benz, A. O., Doty, S. D., van Dishoeck, E. F., & Bourke, T. L. 2009a, *ApJ*, 700, 872
- Bruderer, S., Benz, A. O., Stäuber, P., & Doty, S. D. 2010a, *ApJ*, 720, 1432
- Bruderer, S., Doty, S. D., & Benz, A. O. 2009b, *ApJS*, 183, 179
- Bruderer, S., et al. 2010b, *A&A*, 521, L44
- Butner, H. M., Evans, N. J., II, Harvey, P. M., Mundy, L. G., Natta, A., & Randich, M. S. 1990, *ApJ*, 364, 164
- Butner, H. M., Evans, N. J., II, Lester, D. F., Levreault, R. M., & Strom, S. E. 1991, *ApJ*, 376, 636
- Carey, S. J., Clark, F. O., Egan, M. P., Price, S. D., Shipman, R. F., & Kuchar, T. A. 1998, *ApJ*, 508, 721
- Carr, J. S., & Najita, J. R. 2008, *Science*, 319, 1504
- Caselli, P., Walmsley, C. M., Tafalla, M., Dore, L., & Myers, P. C. 1999, *ApJ*, 523, L165
- Caselli, P., Walmsley, C. M., Zucconi, A., Tafalla, M., Dore, L., & Myers, P. C. 2002, *ApJ*, 565, 331
- Caselli, P., et al. 2010, *A&A*, 521, L29
- Ceccarelli, C., Castets, A., Caux, E., Hollenbach, D., Loinard, L., Molinari, S., & Tielens, A. G. G. M. 2000a, *A&A*, 355, 1129
- Ceccarelli, C., Hollenbach, D. J., & Tielens, A. G. G. M. 1996, *ApJ*, 471, 400
- Ceccarelli, C., Loinard, L., Castets, A., Tielens, A. G. G. M., & Caux, E. 2000b, *A&A*, 357, L9
- Ceccarelli, C., et al. 1999, *A&A*, 342, L21
- . 2010, *A&A*, 521, L22
- Cernicharo, J., & Crovisier, J. 2005, *Space Sc. Rev.*, 119, 29
- Cernicharo, J., Thum, C., Hein, H., John, D., Garcia, P., & Mattiocco, F. 1990, *A&A*, 231, L15
- Cernicharo, J., et al. 2006, *ApJ*, 649, L33
- Cesaroni, R., Hofner, P., Walmsley, C. M., & Churchwell, E. 1998, *A&A*, 331, 709
- Cesaroni, R., Neri, R., Olmi, L., Testi, L., Walmsley, C. M., & Hofner, P. 2005, *A&A*, 434, 1039

- Chandler, C. J., Brogan, C. L., Shirley, Y. L., & Loinard, L. 2005, *ApJ*, 632, 371
- Charnley, S. B. 1997, *ApJ*, 481, 396
- Chavarría, L., et al. 2010, *A&A*, 521, L37
- Chen, J., Evans, N. J., Lee, J., & Bourke, T. L. 2009, *ApJ*, 705, 1160
- Chen, X., Launhardt, R., Bourke, T. L., Henning, T., & Barnes, P. J. 2008, *ApJ*, 683, 862
- Cheung, A. C., Rank, D. M., & Townes, C. H. 1969, *Nature*, 221, 626
- Codella, C., et al. 2010, *A&A*, 518, L112
- Crapsi, A., Caselli, P., Walmsley, C. M., Myers, P. C., Tafalla, M., Lee, C. W., & Bourke, T. L. 2005, *ApJ*, 619, 379
- Crapsi, A., van Dishoeck, E. F., Hogerheijde, M. R., Pontoppidan, K. M., & Dullemond, C. P. 2008, *A&A*, 486, 245
- Crimier, N., Ceccarelli, C., Maret, S., Bottinelli, S., Caux, E., Kahane, C., Lis, D. C., & Olofsson, J. 2010, *A&A*, 519, A65
- Cuppen, H. M., Ioppolo, S., Romanzin, C., & Linnartz, H. 2010, *Chem. Phys.*, 12, 12077
- Dalgarno, A., & Black, J. H. 1976, *Rep. Prog. Phys.*, 39, 573
- Daniel, F., Dubernet, M., Pacaud, F., & Grosjean, A. 2010, *A&A*, 517, A13
- Dartois, E., Thi, W., Geballe, T. R., Deboffle, D., d'Hendecourt, L., & van Dishoeck, E. 2003, *A&A*, 399, 1009
- De Buizer, J. M., & Minier, V. 2005, *ApJ*, 628, L151
- de Geus, E. J., Bronfman, L., & Thaddeus, P. 1990, *A&A*, 231, 137
- de Graauw, T., et al. 2010, *A&A*, 518, L6
- Dick, M., Drouin, B., & Pearson, J. 2010, *Phys. Rev.*, A, 81
- Di Francesco, J., Johnstone, D., Kirk, H., MacKenzie, T., & Ledwosinska, E. 2008, *ApJS*, 175, 277
- Dominik, C., Ceccarelli, C., Hollenbach, D., & Kaufman, M. 2005, *ApJ*, 635, L85
- Doty, S. D., & Neufeld, D. A. 1997, *ApJ*, 489, 122
- Doty, S. D., Schöier, F. L., & van Dishoeck, E. F. 2004, *A&A*, 418, 1021
- Doty, S. D., van Dishoeck, E. F., & Tan, J. C. 2006, *A&A*, 454, L5
- Doty, S. D., van Dishoeck, E. F., van der Tak, F. F. S., & Boonman, A. M. S. 2002, *A&A*, 389, 446
- Dubernet, M., Daniel, F., Grosjean, A., & Lin, C. Y. 2009, *A&A*, 497, 911
- Dubernet, M., et al. 2006, *A&A*, 460, 323
- Dulieu, F., Amiaud, L., Congiu, E., Fillion, J., Matar, E., Momeni, A., Pirronello, V., & Lemaire, J. L. 2010, *A&A*, 512, A30
- Dullemond, C. P., & Dominik, C. 2004, *A&A*, 417, 159
- Dzib, S., Loinard, L., Mioduszewski, A. J., Boden, A. F., Rodríguez, L. F., & Torres, R. M. 2010, *ApJ*, 718, 610
- Eiroa, C., Palacios, J., & Casali, M. M. 1998, *A&A*, 335, 243
- Elitzur, M., & Watson, W. D. 1978, *ApJ*, 222, L141
- Evans, N. J., et al. 2009, *ApJS*, 181, 321
- Evans, N. J., II, et al. 2003, *PASP*, 115, 965
- Fich, M., et al. 2010, *A&A*, 518, L86
- Franklin, J., Snell, R. L., Kaufman, M. J., Melnick, G. J., Neufeld, D. A., Hollenbach, D. J., & Bergin, E. A. 2008, *ApJ*, 674, 1015
- Fraser, H. J., Collings, M. P., McCoustra, M. R. S., & Williams, D. A. 2001, *MNRAS*, 327, 1165
- Froebrich, D. 2005, *ApJS*, 156, 169
- Fuente, A., Neri, R., & Caselli, P. 2005a, *A&A*, 444, 481
- Fuente, A., Rizzo, J. R., Caselli, P., Bachiller, R., & Henkel, C. 2005b, *A&A*, 433, 535
- Garay, G., Brooks, K. J., Mardones, D., Norris, R. P., & Burton, M. G. 2002, *ApJ*, 579, 678
- Gensheimer, P. D., Mauersberger, R., & Wilson, T. L. 1996, *A&A*, 314, 281
- Gerin, M., et al. 2010, *A&A*, 518, L110
- Giannini, T., McCoe, C., Nisini, B., Cabrit, S., Caratti o Garatti, A., Calzoletti, L., & Flower, D. R. 2006, *A&A*, 459, 821
- Giannini, T., Nisini, B., & Lorenzetti, D. 2001, *ApJ*, 555, 40
- Giannini, T., et al. 2005, *A&A*, 433, 941
- Gibb, E. L., Whittet, D. C. B., Boogert, A. C. A., & Tielens, A. G. G. M. 2004b, *ApJS*, 151, 35
- Gibb, A. G., Wyrowski, F., & Mundy, L. G. 2004a, *ApJ*, 616, 301
- Goldsmith, P. F., & Langer, W. D. 1978, *ApJ*, 222, 881
- Green, S., Maluendes, S., & McLean, A. D. 1993, *ApJS*, 85, 181
- Gullixson, C., Gehr, R. D., Hackwell, J. A., Grasdalen, G. L., & Castelaz, M. 1983, *ApJS*, 53, 413
- Gupta, H., et al. 2010, *A&A*, 521, L47
- Gustafsson, M., Ravkilde, T., Kristensen, L. E., Cabrit, S., Field, D., & Pineau Des Foëts, G. 2010, *A&A*, 513, A5
- Hachisuka, K., et al. 2006, *ApJ*, 645, 337
- Hartogh, P., et al. 2010, *A&A*, 518, L150
- Harwit, M., Neufeld, D. A., Melnick, G. J., & Kaufman, M. J. 1998, *ApJ*, 497, L105
- Helmich, F. P., et al. 1996, *A&A*, 315, L173
- Herbst, E., & Klemperer, W. 1973, *ApJ*, 185, 505
- Herbst, E., & van Dishoeck, E. F. 2009, *ARA&A*, 47, 427
- Hersant, F., Wakelam, V., Dutrey, A., Guilloteau, S., & Herbst, E. 2009, *A&A*, 493, L49
- Hirota, T., et al. 2008, *PASJ*, 60, 37
- Hjalmarsen, Å., et al. 2003, *A&A*, 402, L39
- Hogerheijde, M. R., van Dishoeck, E. F., Blake, G. A., & van Langevelde, H. J. 1997, *ApJ*, 489, 293
- Hogerheijde, M. R., van Dishoeck, E. F., Salverda, J. M., & Blake, G. A. 1999, *ApJ*, 513, 350
- Hogerheijde, M. R., & van der Tak, F. F. S. 2000, *A&A*, 362, 697
- Hollenbach, D., Kaufman, M. J., Bergin, E. A., & Melnick, G. J. 2009, *ApJ*, 690, 1497
- Hollenbach, D., & McKee, C. F. 1989, *ApJ*, 342, 306
- Hübers, H. W., Evenson, K. M., Hill, C., & Brown, J. M. 2009, *J. Chem. Phys.*, 131, 034311
- Hunter, T. R., Brogan, C. L., Indebetouw, R., & Cyganowski, C. J. 2008, *ApJ*, 680, 1271
- Ioppolo, S., Cuppen, H. M., Romanzin, C., van Dishoeck, E. F., & Linnartz, H. 2008, *ApJ*, 686, 1474
- . 2010, *Phys. Chem. Chem. Phys.*, 12, 12065
- Ivezić, Z., & Elitzur, M. 1997, *MNRAS*, 287, 799
- Jacq, T., Walmsley, C. M., Henkel, C., Baudry, A., Mauersberger, R., & Jewell, P. R. 1990, *A&A*, 228, 447
- Johnstone, D., Fich, M., Mitchell, G. F., & Moriarty-Schieven, G. 2001, *ApJ*, 559, 307
- Johnstone, D., et al. 2010, *A&A*, 521, L41
- Jørgensen, J. K. 2004, *A&A*, 424, 589
- Jørgensen, J. K., Bourke, T. L., Myers, P. C., Schöier, F. L., van Dishoeck, E. F., & Wilner, D. J. 2005a, *ApJ*, 632, 973
- Jørgensen, J. K., Johnstone, D., van Dishoeck, E. F., & Doty, S. D. 2006, *A&A*, 449, 609

- Jørgensen, J. K., Schöier, F. L., & van Dishoeck, E. F. 2002, *A&A*, 389, 908
- . 2004, *A&A*, 416, 603
- . 2005b, *A&A*, 437, 501
- Jørgensen, J. K., & van Dishoeck, E. F. 2010a, *ApJ*, 710, L72
- . 2010b, *ApJ*, 725, L172
- Jørgensen, J. K., van Dishoeck, E. F., Visser, R., Bourke, T. L., Wilner, D. J., Lommen, D., Hogerheijde, M. R., & Myers, P. C. 2009, *A&A*, 507, 861
- Jørgensen, J. K., et al. 2007, *ApJ*, 659, 479
- Kaufman, M. J., & Neufeld, D. A. 1996, *ApJ*, 456, 611
- Keene, J., Phillips, T. G., & van Dishoeck, E. F. 1997, in *IAU Symp.* 170, CO: Twenty-Five Years of Millimeter-Wave Spectroscopy (Dordrecht: Kluwer), 382
- Keto, E., & Caselli, P. 2010, *MNRAS*, 402, 1625
- Keto, E., Rybicki, G. B., Bergin, E. A., & Plume, R. 2004, *ApJ*, 613, 355
- Klippenstein, S. J., Georgievskii, Y., & McCall, B. J. 2010, *J. Phys. Chem. A*, 114, 278
- Knude, J., & Hog, E. 1998, *A&A*, 338, 897
- Kristensen, L. E., van Dishoeck, E. F., van Kempen, T. A., Cuppen, H. M., Brinch, C., Jørgensen, J. K., & Hogerheijde, M. R. 2010a, *A&A*, 516, A57
- Kristensen, L. E., et al. 2010b, *A&A*, 521, L30
- Ladd, E. F., Deane, J. R., Sanders, D. B., & Wynn-Williams, C. G. 1993, *ApJ*, 419, 186
- Lee, J., Bergin, E. A., & Evans, N. J., II 2004, *ApJ*, 617, 360
- Lefloch, B., et al. 2010, *A&A*, 518, L113
- Lis, D. C., et al. 2010, *A&A*, 521, L26
- Liseau, R., Lorenzetti, D., Nisini, B., Spinoglio, L., & Moneti, A. 1992, *A&A*, 265, 577
- Liu, F., et al. 2010, *A&A* in press
- Loinard, L., Castets, A., Ceccarelli, C., Caux, E., & Tielens, A. G. G. M. 2001, *ApJ*, 552, L163
- Lommen, D., Jørgensen, J. K., van Dishoeck, E. F., & Crapsi, A. 2008, *A&A*, 481, 141
- Maret, S., Ceccarelli, C., Caux, E., Tielens, A. G. G. M., & Castets, A. 2002, *A&A*, 395, 573
- Maret, S., Ceccarelli, C., Tielens, A. G. G. M., Caux, E., Lefloch, B., Faure, A., Castets, A., & Flower, D. R. 2005, *A&A*, 442, 527
- Marseille, M., Bontemps, S., Herpin, F., van der Tak, F. F. S., & Purcell, C. R. 2008, *A&A*, 488, 579
- Marseille, M. G., et al. 2010, *A&A*, 521, L32
- Meeus, G., Waters, L. B. F. M., Bouwman, J., vandenAncker, M. E., Waelkens, C., & Malfait, K. 2001, *A&A*, 365, 476
- Melnick, G. J. 2009, in *ASP Conf. Ser.* 417, Submillimeter Astrophysics and Technology: A Symposium Honoring Thomas G. Phillips (San Francisco: ASP), 59
- Melnick, G. J., Tolls, V., Neufeld, D. A., Yuan, Y., Sonnentrucker, P., Watson, D. M., Bergin, E. A., & Kaufman, M. J. 2008, *ApJ*, 683, 876
- Melnick, G. J., et al. 2000, *ApJ*, 539, L77
- Menten, K. M., Wyrowski, F., Belloche, A., Güsten, R., Dedes, L., & Müller, H. S. P. 2011, *A&A*, 525, A77
- Miyauchi, N., Hidaka, H., Chigai, T., Nagaoka, A., Watanabe, N., & Kouchi, A. 2008, *Chem. Phys. Lett.*, 456, 27
- Molinari, S., Brand, J., Cesaroni, R., & Palla, F. 1996, *A&A*, 308, 573
- Mookerjee, B., Casper, E., Mundy, L. G., & Looney, L. W. 2007, *ApJ*, 659, 447
- Motte, F., Bontemps, S., Schilke, P., Schneider, N., Menten, K. M., & Brogière, D. 2007, *A&A*, 476, 1243
- Motte, F., Schilke, P., & Lis, D. C. 2003, *ApJ*, 582, 277
- Mozurkewich, D., Schwartz, P. R., & Smith, H. A. 1986, *ApJ*, 311, 371
- Mueller, K. E., Shirley, Y. L., Evans, N. J., II, & Jacobson, H. R. 2002, *ApJS*, 143, 469
- Müller, H. S. P., Thorwirth, S., Roth, D. A., & Winnewisser, G. 2001, *A&A*, 370, L49
- Mürtz, P., Zink, L. R., Evenson, K. M., & Brown, J. M. 1998, *J. Chem. Phys.*, 109, 9744
- Neufeld, D. A., & Dalgarno, A. 1989, *ApJ*, 344, 251
- Neufeld, D. A., & Kaufman, M. J. 1993, *ApJ*, 418, 263
- Neufeld, D. A., et al. 2009, *ApJ*, 706, 170
- . 2010, *A&A*, 521, L10
- Nisini, B., Antonucci, S., Giannini, T., & Lorenzetti, D. 2005, *A&A*, 429, 543
- Nisini, B., Benedettini, M., Giannini, T., Codella, C., Lorenzetti, D., di Giorgio, A. M., & Richer, J. S. 2000, *A&A*, 360, 297
- Nisini, B., Codella, C., Giannini, T., Santiago Garcia, J., Richer, J. S., Bachiller, R., & Tafalla, M. 2007, *A&A*, 462, 163
- Nisini, B., Giannini, T., & Lorenzetti, D. 2002, *ApJ*, 574, 246
- Nisini, B., et al. 2010, *A&A*, 518, L120
- Noriega-Crespo, A., et al. 2004, *ApJS*, 154, 352
- Öberg, K. I., Fuchs, G. W., Awad, Z., Fraser, H. J., Schlemmer, S., van Dishoeck, E. F., & Linnartz, H. 2007, *ApJ*, 662, L23
- Öberg, K. I., Linnartz, H., Visser, R., & van Dishoeck, E. F. 2009, *ApJ*, 693, 1209
- Olberg, M. 2010, Tech. Note ICC/2010-nnn (Groningen: HIFI ICC), http://herschel.esac.esa.int/Docs/TechnicalNotes/HIFI_Beam_Efficiencies_17Nov2010.pdf
- Olmi, L., Cesaroni, R., & Walmsley, C. M. 1996, *A&A*, 307, 599
- Ossenkopf, V., et al. 2010, *A&A*, 518, L111
- Ott, S., et al. 2010, in *ASP Conf. Ser.* 434, Astronomical Data Analysis Software and Systems XIX, ed. Y. Mizumoto, K.-I. Morita, & M. Ohishi (San Francisco: ASP), 139
- Parise, B., Castets, A., Herbst, E., Caux, E., Ceccarelli, C., Mukhopadhyay, I., & Tielens, A. G. G. M. 2004, *A&A*, 416, 159
- Parise, B., Ceccarelli, C., & Maret, S. 2005a, *A&A*, 441, 171
- Parise, B., Simon, T., Caux, E., Dartois, E., Ceccarelli, C., Rayner, J., & Tielens, A. G. G. M. 2003, *A&A*, 410, 897
- Parise, B., et al. 2005b, *A&A*, 431, 547
- Persson, C. M., et al. 2007, *A&A*, 476, 807
- Phillips, T. G., van Dishoeck, E. F., & Keene, J. 1992, *ApJ*, 399, 533
- Phillips, T. R., Maluendes, S., & Green, S. 1996, *ApJS*, 107, 467
- Pickett, H. M., Poynter, I. R. L., Cohen, E. A., Delitsky, M. L., Pearson, J. C., & Muller, H. S. P. 1998, *J. Quant. Spectrosc. Radiat. Transf.*, 60, 883
- Pilbratt, G. L., et al. 2010, *A&A*, 518, L1
- Pillai, T., Wyrowski, F., Carey, S. J., & Menten, K. M. 2006a, *A&A*, 450, 569
- Pillai, T., Wyrowski, F., Menten, K. M., & Krügel, E. 2006b, *A&A*, 447, 929
- Plume, R., et al. 2004, *ApJ*, 605, 247
- Poelman, D. R., & Spaans, M. 2005, *A&A*, 440, 559
- Poelman, D. R., & van der Tak, F. F. S. 2007, *A&A*, 475, 949

- Poglitsch, A., et al. 2010, *A&A*, 518, L2
- Polehampton, E. T., Baluteau, J., Swinyard, B. M., Goicoechea, J. R., Brown, J. M., White, G. J., Cernicharo, J., & Grundy, T. W. 2007, *MNRAS*, 377, 1122
- Pontoppidan, K. M., Salyk, C., Blake, G. A., Meijerink, R., Carr, J. S., & Najita, J. 2010, *ApJ*, 720, 887
- Pontoppidan, K. M., van Dishoeck, E. F., & Dartois, E. 2004, *A&A*, 426, 925
- Ralchenko, Y., Kramida, A. E., Reader, J., & NIST ASD Team 2008, *NIST Atomic Spectra Database (v3.1.5)*, <http://physics.nist.gov/asd3>
- Raymond, S. N., Quinn, T., & Lunine, J. I. 2004, *Icarus*, 168, 1
- Roberts, H., Herbst, E., & Millar, T. J. 2003, *ApJ*, 591, L41
- Roberts, H., & Millar, T. J. 2007, *A&A*, 471, 849
- Robitaille, T. P., Whitney, B. A., Indebetouw, R., Wood, K., & Denzmore, P. 2006, *ApJS*, 167, 256
- Rodgers, S. D., & Charnley, S. B. 2003, *ApJ*, 585, 355
- Rodón, J. A., Beuther, H., Megeath, S. T., & van der Tak, F. F. S. 2008, *A&A*, 490, 213
- Romanzin, C., et al. 2010, *MNRAS* in press
- Sakai, N., Sakai, T., Hirota, T., Burton, M., & Yamamoto, S. 2009, *ApJ*, 697, 769
- Salyk, C., Pontoppidan, K. M., Blake, G. A., Lahuis, F., van Dishoeck, E. F., & Evans, N. J., II 2008, *ApJ*, 676, L49
- Sandell, G. 2000, *A&A*, 358, 242
- Sandell, G., & Sievers, A. 2004, *ApJ*, 600, 269
- Schilke, P., et al. 2010, *A&A*, 521, L11
- Schöier, F. L., Jørgensen, J. K., van Dishoeck, E. F., & Blake, G. A. 2002, *A&A*, 390, 1001
- . 2004, *A&A*, 418, 185
- Schöier, F. L., van der Tak, F. F. S., van Dishoeck, E. F., & Black, J. H. 2005, *A&A*, 432, 369
- Schulz, A., Guesten, R., Walmsley, C. M., & Serabyn, E. 1991, *A&A*, 246, L55
- Seidensticker, K. J., & Schmidt-Kaler, T. 1989, *A&A*, 225, 192
- Shevchenko, V. S., & Yakubov, S. D. 1989, *Soviet Astron.*, 33, 370
- Shu, F. H., Adams, F. C., & Lizano, S. 1987, *ARA&A*, 25, 23
- Slawson, R. W., & Reed, B. C. 1988, *AJ*, 96, 988
- Snell, R. L., Hollenbach, D., Howe, J. E., Neufeld, D. A., Kaufman, M. J., Melnick, G. J., Bergin, E. A., & Wang, Z. 2005, *ApJ*, 620, 758
- Snell, R. L., Scoville, N. Z., Sanders, D. B., & Erickson, N. R. 1984, *ApJ*, 284, 176
- Snell, R. L., et al. 2000, *ApJ*, 539, L101
- Sollins, P. K., et al. 2004, *ApJ*, 616, L35
- Sridharan, T. K., Beuther, H., Schilke, P., Menten, K. M., & Wyrowski, F. 2002, *ApJ*, 566, 931
- Stanke, T., McCaughrean, M. J., & Zinnecker, H. 2000, *A&A*, 355, 639
- Stäuber, P., Doty, S. D., van Dishoeck, E. F., & Benz, A. O. 2005, *A&A*, 440, 949
- Stäuber, P., Doty, S. D., van Dishoeck, E. F., Jørgensen, J. K., & Benz, A. O. 2004, *A&A*, 425, 577
- Stäuber, P., Jørgensen, J. K., van Dishoeck, E. F., Doty, S. D., & Benz, A. O. 2006, *A&A*, 453, 555
- Sturm, B., et al. 2010, *A&A*, 518, L129
- Szymczak, M., Pillai, T., & Menten, K. M. 2005, *A&A*, 434, 613
- Tafalla, M., Mardones, D., Myers, P. C., Caselli, P., Bachiller, R., & Benson, P. J. 1998, *ApJ*, 504, 900
- Tafalla, M., Santiago-García, J., Myers, P. C., Caselli, P., Walmsley, C. M., & Crapsi, A. 2006, *A&A*, 455, 577
- Takahashi, T., Silk, J., & Hollenbach, D. J. 1983, *ApJ*, 275, 145
- Tamura, M., Gatley, I., Waller, W., & Werner, M. W. 1991, *ApJ*, 374, L25
- Thi, W. F., et al. 2001, *ApJ*, 561, 1074
- Tielens, A. G. G. M., & Hagen, W. 1982, *A&A*, 114, 245
- Valiron, P., Wernli, M., Faure, A., Wiesenfeld, L., Rist, C., Kedzuch, S., & Noga, J. 2008, *J. Chem. Phys.*, 129
- van der Tak, F. F. S., Black, J. H., Schöier, F. L., Jansen, D. J., & van Dishoeck, E. F. 2007, *A&A*, 468, 627
- van der Tak, F. F. S., van Dishoeck, E. F., & Caselli, P. 2000a, *A&A*, 361, 327
- van der Tak, F. F. S., van Dishoeck, E. F., Evans, N. J., II, Bakker, E. J., & Blake, G. A. 1999, *ApJ*, 522, 991
- van der Tak, F. F. S., van Dishoeck, E. F., Evans, N. J., II, & Blake, G. A. 2000b, *ApJ*, 537, 283
- van der Tak, F. F. S., Walmsley, C. M., Herpin, F., & Ceccarelli, C. 2006, *A&A*, 447, 1011
- van der Tak, F. F. S., et al. 2010, *A&A*, 518, L107
- van der Werf, P. P., et al. 2010, *A&A*, 518, L42
- van Dishoeck, E. F. 2004, *ARA&A*, 42, 119
- van Dishoeck, E. F., Blake, G. A., Jansen, D. J., & Groesbeck, T. D. 1995, *ApJ*, 447, 760
- van Dishoeck, E. F., & Helmich, F. P. 1996, *A&A*, 315, L177
- van Kempen, T. A., Doty, S. D., van Dishoeck, E. F., Hogerheijde, M. R., & Jørgensen, J. K. 2008, *A&A*, 487, 975
- van Kempen, T. A., van Dishoeck, E. F., Hogerheijde, M. R., & Güsten, R. 2009a, *A&A*, 508, 259
- van Kempen, T. A., van Dishoeck, E. F., Salter, D. M., Hogerheijde, M. R., Jørgensen, J. K., & Boogert, A. C. A. 2009b, *A&A*, 498, 167
- van Kempen, T. A., Wilner, D., & Gurwell, M. 2009c, *ApJ*, 706, L22
- van Kempen, T. A., et al. 2009d, *A&A*, 501, 633
- . 2009e, *A&A*, 507, 1425
- . 2010a, *A&A*, 518, L128
- . 2010b, *A&A*, 518, L121
- van Zadelhoff, G., et al. 2002, *A&A*, 395, 373
- Vejby-Christensen, L., Andersen, L. H., Heber, O., Kella, D., Pedersen, H. B., Schmidt, H. T., & Zajfman, D. 1997, *ApJ*, 483, 531
- Velusamy, T., Langer, W. D., & Marsh, K. A. 2007, *ApJ*, 668, L159
- Visser, R., van Dishoeck, E. F., Doty, S. D., & Dullemond, C. P. 2009, *A&A*, 495, 881
- Viti, S., Roueff, E., Hartquist, T. W., Pineau des Forêts, G., & Williams, D. A. 2001, *A&A*, 370, 557
- Viti, S., & Williams, D. A. 1999, *MNRAS*, 305, 755
- Walmsley, M., & van der Tak, F. 2005, in *Dusty and Molecular Universe: A Prelude to Herschel and ALMA*, ed. A. Wilson (ESA SP-577; Noordwijk: ESA), 55
- Wampfler, S. F., et al. 2010, *A&A*, 521, L36
- Watson, D. M., et al. 2007, *Nature*, 448, 1026
- Westley, M. S., Baragiola, R. A., Johnson, R. E., & Baratta, G. A. 1995, *Nature*, 373, 405

- Whittet, D. C. B. 2003, *Dust in the Galactic Environment* (Philadelphia: IOP)
- Whittet, D. C. B., Bode, M. F., Longmore, A. J., Adamson, A. J., McFadzean, A. D., Aitken, D. K., & Roche, P. F. 1988, *MNRAS*, 233, 321
- Wiesenfeld, L., & Faure, A. 2010, *Phys. Rev. A*, 82
- Wilking, B. A., Greene, T. P., Lada, C. J., Meyer, M. R., & Young, E. T. 1992, *ApJ*, 397, 520
- Wilson, B. A., Dame, T. M., Mashedier, M. R. W., & Thaddeus, P. 2005, *A&A*, 430, 523
- Wood, D. O. S., & Churchwell, E. 1989, *ApJ*, 340, 265
- Woodall, J., Agúndez, M., Markwick-Kemper, A. J., & Millar, T. J. 2007, *A&A*, 466, 1197
- Wyrowski, F., Menten, K. M., Güsten, R., & Belloche, A. 2010a, *A&A*, 518, A26
- Wyrowski, F., Menten, K. M., Schilke, P., Thorwirth, S., Güsten, R., & Bergman, P. 2006, *A&A*, 454, L91
- Wyrowski, F., et al. 2010b, *A&A*, 521, L34
- Yang, C.-H., et al. 2010, *J. Chem. Phys.*, 11, 11
- Yıldız, U. A., et al. 2010, *A&A*, 521, L40